The puzzle of the 1996 Bárdarbunga earthquake, Iceland: Constraints from kinematic modelling

Hrvoje Tkalčić[1,*], Douglas S. Dreger[2], Gillian R. Foulger[3], Bruce R. Julian[4]

[1]*Multimax, Inc., Emeryville, CA 94608, USA. Tel. (510) 420-1429; E-mail: tkalcic@multimax.com*

[2]*Berkeley Seismological Laboratory, University of California, Berkeley, CA 94720, USA.*

[3]*Department of Earth Sciences, Durham University, Durham DH13LE, UK.*

[4]*U.S. Geological Survey, Menlo Park, CA 94025, USA.*

Accepted *date*. Received *date*; in original form *date*

Abbreviated title: Kinematic modelling of the Bárdarbunga earthquake, Iceland

SUMMARY

A volcanic earthquake with Mw=5.6 occurred beneath the Bárdarbunga volcano caldera in Iceland September 29, 1996. We investigated the event with a complete moment tensor inversion method using long-period seismic waveforms. The resulting moment tensor is characterized by a significant non-double-couple component. The deviatoric inversion we performed using data from stations of the Iceland Hotspot Project yields a non-double-couple solution with a 67% vertically oriented compensated linear vector dipole component, while the full moment tensor solution shows a similar, 66% compensated

linear vector dipole component, 32% double-couple component and a statistically insignificant 2% volumetric (isotropic) contraction.

Utilizing an elastic finite-difference program, with a large number of equidistantly distributed point sources we simulated various rupture histories on the walls of a conical surface representing the Bárdarbunga caldera ring fault and compared them with the observations. We were able to identify the physical characteristics of a rupture scenario that produces synthetic seismograms resembling the observed data to a high level of detail. The best results are for ruptures extending along half the perimeter of the caldera ring fault. The rupture velocity could have been super-shear and we hypothesize that it could have been triggered by compressional waves travelling directly across the caldera, rather than propagating along the curved fault. An alternative scenario involves two offset sources with similar but opposite volume changes. Such a model cannot be ruled out but the circumstances under which it could happen are rare.

Key words: Earthquake-source mechanism, volcanic structure, seismic modelling, synthetic seismograms.

1 INTRODUCTION

A remarkable series of seismic and magmatic events beneath the Vatnajokull icecap in Iceland began in July 1995, and ultimately led to a glacial flood from the Grimsvötn volcano subglacial caldera lake. On September 29, 1996, a sequence of earthquakes commenced, starting with a magnitude 5.6 earthquake in the Bárdarbunga volcano (Fig. 1). Similar earthquakes had occurred in this area of Iceland previously. However this time the event was followed by a swarm of small earthquakes that extended to the neighbouring volcano Grímsvötn, indicating widespread volcanic activation.

The main event, a magnitude 5.6 earthquake, displayed an unusual pattern of seismic radiation, suggesting a mechanism that could not be explained with purely double couple (DC) forces (Section 2). In fact, studies of the event using teleseismic long-period and intermediate period surface wave data (Nettles & Ekström 1998) and Icelandic data with a simple 1D-averaged velocity model (Konstantinou *et al*. 2003) revealed solutions that are best described as a CLVD and a mechanism in which a dominant vertically oriented vector dipole is in tension. Konstantinou *et al*. (2003) also reported a small (8.5%) implosive ISO component and concluded that it was statistically significant. Nettles & Ekström (1998) proposed that the derived NDC source mechanisms are consistent with the tectonic setting of the region. They hypothesized that they are the result of a sequence of sub-events of varying geometry, faulting on an outward dipping cone-shaped ring fault beneath the caldera, as a result of a change in pressure in the volcano's shallow magma chamber.

Here we determine the complete seismic moment tensor and find that there is no

statistically significant isotropic component. The most likely physical explanations for the lack of a volumetric component are tectonic slip on conically shaped walls of the caldera or a mass-exchange mechanism that would produce net zero volumetric component. We simulate a finite-source process on a conical ring fault to evaluate the conditions under which a faulting origin of the event is viable. In addition, we examine the mass exchange hypothesis in view of the lack of a significant volumetric component in the source.

2 A NON-DOUBLE-COUPLE SEISMIC SOURCE

DC forces are fictitious forces that would generate, in a medium without discontinuity, the same elastic field that is generated by the dislocation at the source. It is a conventional way of representing a point source model (e.g. Kostrov and Das 1989). Purely DC point source models consist of two vector dipoles resulting in quadrant-like distribution of the signs of first arrivals (two nodal planes perpendicular one to another, which when projected to the surface resemble the so called “beach-ball”). Seismic moment M_{ij} provides a general representation of the seismic source. Due to the complex nature of earthquake processes, especially for non-tectonic environments, M_{ij} is better represented by decomposition into DC, CLVD and ISO components. This is the approach we adopted in our analysis of the Bárdarbunga earthquake.

The CLVD corresponds to a combination of dipoles that can describe different (non-DC) physical events without net change in volume. The dominant dipole is double in strength and opposite in sign to the two minor, orthogonal dipoles and it can be either compressional or dilatational. A pure CLVD point source results in a cylindrical nodal

plane which, when projected onto a sphere and presented as a "beach ball", resembles a circle inside a circle. The ISO component resolves the volumetric changes. The CLVD component of a tectonic earthquake typically contains less than 30% of the total seismic moment. In the case of the Bárdarbunga earthquake, the CLVD component is dominant over the DC component and involves an outward-orientated, vertical major dipole (vertical tension).

NDC earthquakes involving CLVD components have been attributed to several physical mechanisms. These include tensile failure (e.g. Julian 1983; Foulger & Long 1984; Julian & Sipkin 1985), complex faulting such as multiple ruptures on a transform fault or mid-ocean ridge (Kawakatsu 1991), or non-planar rupture (Kuge & Lay 1994; Frolich 1994; Julian *et al.* 1998). In addition, dip-slip shear faulting on a conical fault spanning a significant azimuth range theoretically also has a NDC component (Frolich 1994; Julian *et al.* 1998; Ekström 1994). This latter mechanism is a possible candidate for the September 29, 1996 event. We test this hypothesis through numerical simulation of the finite rupture process for an outward-dipping ring fault using a 3D finite-difference method.

3 SEISMIC DATA AND VELOCITY MODELS FOR ICELAND

A useful dataset with which to study the event was collected by the regional scale Iceland Hotspot IRIS-PASSCAL seismic experiment (Foulger et al., 2001). Studies using these data have shown the high level of complexity of crustal structure beneath Iceland. For example, teleseismic receiver functions and surface-wave dispersion measurements have been used to obtain the laterally varying velocity structure beneath Iceland (Du &

Foulger 1999, 2001; Du et al., 2002). Crustal thickness has been determined using a combination of seismic profiles, receiver functions and gravity profiles (Darbyshire *et al.* 1999; Foulger et al., 2003). Another study used seismic tomography to constrain the structure under Iceland (Foulger et al., 1999; 2001). These studies demonstrated the high level of complexity of crustal structure beneath Iceland.

In the case of the present study, the most difficult task was calculation and calibration of Green's functions for the Iceland area. Utilizing a frequency wave-number integration (FKI) program, we produced a set of Green's functions for a) a radially averaged S-wave crustal tomography model (Allen *et al.* 2002) and b) crustal models determined by jointly inverting for teleseismic receiver functions and surface wave dispersion curves (Du & Foulger, 1999). Using one single velocity model for Iceland to estimate Green's functions for all source-receiver path combinations did not yield high-percentage fits for the observed waveforms, especially when waveforms from more than 2 stations were inverted for. We obtained significantly better results when distinctive velocity models from the results of Du & Foulger (1999) were used to produce the Green's functions between the source and various station locations. This was true in our case despite the fact that teleseismic receiver functions are sensitive only to the structure under a receiver (with some lateral sensitivity), while Green's functions represent the response of the layered structure between the source and a receiver. We found that our approach resulted in a superior fit of the synthetic seismograms to the regional data collected by the Iceland Hotspot Project.

4 FULL MOMENT TENSOR INVERSION

In order to invert for the moment tensor, we used the full waveform inversion method described by Pasyanos *et al.* (1996). Both deviatoric (where M_{ij} is decomposed into only DC and CLVD components) and full moment tensor (FMT) solutions were obtained for the Bárdarbunga earthquake. The FMT inversion allows for an isotropic process (explosion or collapse) and recovery of such a component is strong evidence for direct fluid involvement in the source process. The method inverts three-component, long period (0.02-0.05 Hz) seismograms for the six independent elements of the seismic moment tensor. An impulsive source time function and a point source are assumed, and depth is inverted for through an iterative process. Using this method, we previously demonstrated the existence of large volumetric components in earthquakes from the Long Valley Caldera, California (Dreger *et al.* 2000). Several studies have demonstrated that the method retrieves a solution that is insensitive to lateral and vertical inhomogeneities along ray paths and near-source or near-receiver structure, but is sensitive to the source orientation and depth for the pass-band employed by the inversion method (e.g. Dreger & Helmberger 1993; Panning *et al.* 2001).

We examined waveform data from all those available from Iceland Hotspot Project stations. For the bulk of the analysis presented in later sections we selected only six stations with excellent azimuthal coverage: HOT01, HOT12, HOT17, HOT22, HOT24 and HOT29 (Fig. 1). The deviatoric inversion of data from these stations yielded an NDC solution with a 67% CLVD component (Fig. 2a), while the FMT resulted in a similar, 66% CLVD component, accompanied by an insignificant volumetric contraction (ISO=2%; Fig. 2b). Inversions using data from other groups of stations revealed that the result is stable and well constrained. One such configuration of stations and

corresponding best fits are shown in Fig. 3. This demonstrates the robustness of the moment tensor solution for the Bárdarbunga earthquake. This was achieved as a result of the good azimuthal coverage and good structural models.

Nettles & Ekström (1998) depth estimate of 3.5 km is based on a broadband analysis for depth and duration of moment release. At the high frequencies, we estimated the nucleation depth of the event to 3.9 km from first arrival travel time analysis. At the low frequencies, in the moment tensor inversion, we tested 1.5, 3.5 and 5.5 km depths and obtained the best results for 3.5 km depth. The depth estimates generally agree well in the different frequency bands.

We performed a sensitivity test where we examined the stability of the CLVD component (expressed as the value of ε, defined as a measure of the size of the CLVD component; Fig. 4a) and ISO (Fig. 4b) as a function of the number of stations used in the inversion. We found that six was the optimal number of stations to resolve any possible ISO component. As can be seen from Fig. 4, after the number of the waveforms increases to three, the strength of the CLVD component becomes invariant with number of new waveforms added, reaching a value of about 0.35. It is also worth noticing that the overall variance reduction does not decrease significantly with the addition of stations. While for a single station the variance reduction can reach 90%, this number drops to about 85% for three to four stations and is still slightly over 80% for six stations. On the other hand, the ISO component percentage decreases with increasing number of waveforms used in the inversion. Clearly, one station is insufficient to estimate the strength of the CLVD component, and even three stations still yield a relatively strong (and erroneous) ISO component. Despite the fact that it was shown previously that it is possible to detect

explosive earthquake components with as few as three stations (Dreger and Woods, 2002) the results shown here illustrate the importance of a good azimuthal coverage in the inversions for more complicated source processes. This may indicate a difference in capability of the moment tensor inversion depending on how well Green's functions describe wave propagation for a region. Also in Dreger and Woods (2002) solutions show isotropic components that are large, but they do not result in a significant improvement in fit compared to the very non-DC deviatoric solution.

We considered an additional grid search for the moment tensor M_{ij} decomposed only into DC components, and only into DC and ISO components. We obtained significantly poorer fits to the data. We also looked at the potential biases that could have been introduced by the possible existence of single forces in the physical process. Other representations of the source mechanism handle this problem by decomposing M_{ij} into six standard tensor components and three single-force components (e.g. Chouet *et al*. 2003). The existence of single forces, however, cannot hinder recovery of an ISO component in our inversion. The inversion is linear with an ISO component included in the M_{ij} decomposition so if there was one in reality, it would have been retrieved.

The issue becomes serious in the cases where a large ISO is retrieved. Our tests show that if a single force dominates the mechanism, the inversion we apply could produce a large false ISO component. This is an important point, however it is not of concern for the Bárdarbunga source mechanism since we do not observe a significant ISO component in our inversion either with or without inverting for single forces.

Recovery of a statistically significant ISO component could be an indicator of a fluid-controlled source process, e.g. dike injection. A small ISO component that we identified

in the FMT solution is not statistically significant as determined by an F-test. Since the mechanism for this event appears to be strongly NDC without a large ISO component, we first test scenarios in which the event could have resulted from complex faulting, such as proposed by Nettles & Ekström (1998). Alternatively, we speculate that a net zero volumetric component is possible if the inflation moment equals the deflation moment in a mass-exchange process carried by a fluid flow, causing cancellation.

5 KINEMATIC MODELLING OF THE EVENT USING FINITE DIFFERENCES

The finite-source analysis described below extracts the original source information that can be recovered by the point-source inversion. It reveals the combination of finite-source parameters needed for a mechanism consistent with what was obtained from the Bárdarbunga earthquake data. This analysis also takes into account other characteristics in the data such as waveform duration and the level of the transverse component with respect to the radial and vertical components.

5.1. Finite-source modelling

We use a finite-difference program *e3d* (Larsen & Schultz 1995) to generate synthetic data from simple point source, strike-slip, dip-slip, explosion mechanisms and their compositions. The finite difference propagation program is fourth-order accurate in space and second-order accurate in time. It is based on the elastodynamic formulation of the wave equation on a staggered grid (e.g. Madariaga 1976; Virieaux 1986; Levander 1988). Suites of seismograms for each independent program run were produced, at each of the positions corresponding to the locations of the Iceland Hotspot

Project stations. To produce synthetic Green's functions, we assumed a point source and 1D structure derived for the north-eastern part of Iceland (Du & Foulger, 1999). In the 20 to 50 second period range used in the regional distance seismic moment tensor inversion, this approximation is reasonable. The fictitious data were then inverted for the seismic moment tensor parameters and depth. Initially, we performed a test in which all of the trial fundamental point-source mechanisms were accurately recovered to verify the inversion process.

In the finite source modelling, the caldera is assumed to be part of a conical surface, dipping outward, and the rupture is assumed to take place along the segment between 3 and 5 km of depth. Using realistic scaling and a surface diameter of the Bárdarbunga caldera of 8.5 km (estimated from a geological map), the corresponding diameters at 3 and 5 km depths are 15.5 and 18.5 km, respectively. To simulate finite-source faulting processes on the caldera walls, we use multiple point sources equidistantly distributed over a conical surface, which resembles the surface of a caldera (Fig. 5). In this modelling we initially assume uniform slip distribution and constant rupture velocity, although a range of rupture velocities from sub-shear to super-shear was also tried. Unidirectional and bidirectional lateral propagation as well as a simultaneous vertical drop of the caldera were tested. For multiple source calculations, a single modelling source is described in terms of fault parameters (strike, dip and rake). The input amplitude of each is related to the total seismic moment M_0 through:

$$A = M_0 \Big/ N \int f(t)dt \qquad (1)$$

f(t) is a Gaussian source-time function and *N* is the total number of sources participating in the rupture. The distance between two consecutive modelling sources was

set to slightly less than 0.2 km, which is much less than the minimum wavelength of seismic waves. To ensure continuity of rupture process, the rise time (half duration of the Gaussian function) is set to 1 s, which is more than 10 times longer than the time in which rupture propagates between two modelling sources, producing a kinematically smooth process. Assuming $v_{rupture}=0.9v_s$, at 5 km depth (v_s=3.04 km/s), that time is about 0.07 s.

Fig. 6 is a summary of the variance reduction results for 24 combinations of dipping angles and portions of the rupture of the caldera. We used finite source waveforms obtained using the finite-differences method as synthetic data and 1D Green's functions to fit the data in a point-source time-domain MT inversion. Fig. 6 shows that the mechanisms (vertical CLVD) and fits similar to the observed (about 80% level) were obtained for cases where 25% and 50% of the caldera perimeter were involved in the rupture. This is not surprising because the shorter the rupture, the closer the waveforms are to the point-source-based Green's functions. It is also evident that it is possible to achieve a relatively good fit for a wide range of dipping angles. This is significant because, to our knowledge, only steeply dipping walls have been observed in geological exhumations of calderas. Fig. 7 illustrates focal mechanisms for the same 24 combinations of orientations and portions of the rupture as shown in Fig. 6. For cases where only a quarter of the caldera was involved in rupture, strong DC and weak CLVD components characterize the focal mechanisms. This clearly was not observed for the Bárdarbunga earthquake. Thus, although the best fits are obtained for the quarter-perimeter models, based on the observed and modelled focal mechanisms we favour the half-perimeter rupture scenarios. The simulations we describe below support this view.

The initial simulations were performed for unidirectional lateral ruptures along the caldera walls initially assuming a Rayleigh wave speed for the rupture velocity. Half- and full-length perimeter rupture scenarios generally reproduce the vertically oriented CLVD source mechanism observed for the Bárdarbunga earthquake. The half-length rupture scenario used to produce synthetic data, and modelling with point source synthetics yields a variance reduction and orientation of the P axis similar to those obtained in modeling the real earthquake waveforms (Fig 2b). However, the moment is slightly under-predicted and the CLVD percentage is higher than that in modelling the earthquake. The full-length (conical) rupture results do not fit as well as the half-length results because of the longer source duration (Fig. 8). Bilateral rupture also produces a satisfactory result, the CLVD percentage and variance reduction level being similar to those obtained in modelling the real earthquake waveforms (Fig. 9).

We repeated the same experiment for a quarter-length rupture (Fig. 10). Even though the waveform fits are good (with the variance reduction only slightly less than for the half-length rupture), the DC component dominates the solution, which is not consistent with observation. Therefore, given a sub-shear rupture velocity, the quarter-length case fails because the focal mechanism predicted is incorrect. The full-length case fails because the predicted waveforms are more drawn out in time than in the observations and are not well fit using the point-source moment tensor inversion. The half-length scenario produces the observed percentage of a vertically oriented CLVD with a reasonable fit to the point-source model.

Finally, we tested a “simultaneous caldera drop” scenario (Fig. 11) despite the fact that this violates the causality principle for a fault with a realistic level of frictional stress.

This scenario is also represented by the mechanism denoted by INF in Fig. 12. While still producing high values of variance reduction, tangential components now become close to zero, and the CLVD component becomes close to 100%. Neither of these are observed for the Bárdarbunga earthquake (Fig 2a). It is noted however that a finite upward rupture initiating everywhere along the base of the fault is another possibility that may fit the data. In addition, if non-uniform slip runs are used in may be possible to devise a model with a level of SH radiation consistent with the observed even for instantaneous drop.

5.2. Super-shear rupture speed?

In order to place more constraints on the Bárdarbunga earthquake source mechanism, we quantified the amount of Love wave radiation generated using the ratio of tangential and vector sum of radial and vertical components, or wave energy (integrated squared velocities). We then compared synthetic waveform wave energy estimates with the observed wave energy for sub-shear rupture speeds. Whilst it is possible to simulate waveforms and obtain a mechanism consistent with the observations, the wave energy from the synthetics overestimates the observed wave energy. Since we could not model the observed wave energy for sub-shear rupture speeds, and recent results for some large earthquakes have documented super-shear rupture (Ellsworth *et al.* 2004; Bouchon *et al.* 2000; Bouchon & Vallée 2003), we performed a series of finite-source simulations over a range of rupture velocities from sub-shear to super-shear.

The results of increasing rupture speed simulations are intriguing and illustrated in Fig. 13. We plot the "beach balls" obtained for various speeds of rupture for the half-cone rupture scenario (the corresponding waveform fits and moment tensor solution for the

case of the Rayleigh wave rupture speed (90% of shear wave speed) are shown in Fig. 2b). First, from Fig. 13, it is clearly possible to simulate waveforms and obtain a mechanism consistent with the observations. The faster rupture speeds result in shorter rupture durations that are more consistent with a temporal point source, so the variance reduction increases. The limiting case with infinite rupture speed represents sudden fault rupture or collapse of the caldera and fits the best. There is significant improvement in fit going from sub-shear to super-shear rupture velocity. Above 173% shear velocity (for a Poisson's ratio of 0.25) there remains a more gradual but steady increase in ability to fit the synthetic data and produce a mechanism consistent with what has been found for the earthquake. One physical mechanism for a super-P-wave rupture velocity could be triggering of the rupture by the compressional wave field that travels directly across the caldera. The time at which P waves reach the wall on the opposite side of the caldera is 160% shorter (the path is shorter by a factor of $\pi/2$). This could decrease the rupture duration in comparison with Rayleigh speed rupture by about 300%.

Wave energy in Fig. 13 is normalized so that it could be shown on the same vertical axis as variance reduction. Evidently, this number decreases with increasing rupture speed as shown in Fig. 13 by diamonds. The line marked by stars shows the Love to Rayleigh energy ratio for the Bárdarbunga earthquake. When the source duration is long the SH radiation lobes are not effectively broken down and the wave energy parameter is high. When the source process is faster destructive interference of the SH radiation lobes eliminates the transverse component energy. Under these circumstances the P-SV radiation pattern undergoes constructive interference and the wave energy parameter decreases. The two lines (the row of stars representing the observed wave energy, and the

array of diamonds representing the synthetic wave energy) intersect at a rupture speed of about 140% of the shear wave speed, indicating that the speed must be super-shear to explain the observed wave energy in the recorded data.

For both the half-length and full-length ruptures at super-shear wave speed, unilaterally propagating ruptures in clockwise and counter-clockwise directions result in similar focal mechanisms. Both lengths of rupture produce variance reductions higher than 80% and even higher than 90%, increasing with the rupture speed demonstrating the increasing point-source character with increasing rupture speed. The focal mechanisms resemble the main mechanism obtained for the Bárdarbunga earthquake, with a vertically oriented dominant CLVD and very small ISO component. It is important to note that in addition to the radial and vertical components of the synthetic seismograms matching better with increasing rupture speed, the tangential components also have relatively high amplitudes as observed. However for full-length perimeter ruptures at the speeds just above Rayleigh wave speed, the sign of the CLVD is reversed and the moment is significantly under-predicted (not shown here). Although the shifts in the moment tensor analysis could be manually adjusted so that the correct cycles are fit, the effect of directivity such as in this case can drive the inversion to fit waveforms on the wrong cycles. The sign of the compressional forces switches back to implosion when higher rupture velocities are used in the simulations.

5.3 Mass (volume) exchange model

In Bárdarbunga, the observed episodic occurrence of non-DC earthquakes with vertically oriented CLVD components is striking (see, for example Figure 1 of Nettles &

Ekström 1998). Although we were able to demonstrate that it is possible to reproduce the observed focal mechanism as slip on a ring fault, in practice, outward dipping ring dikes are known to be near-vertical and therefore not very efficient at producing non-double-couple earthquakes. Cone sheets would be more efficient but they dip inward. In addition, there are some indications from smaller aftershocks whose mechanisms we analyzed using Julian (1986) and Julian and Foulger (1996) method, that in at least several cases the focal mechanisms were similar to that for the main event. We therefore considered a mass-exchange process that can yield a non-DC mechanism and still produce a zero volumetric component in the moment tensor inversion. This could be two magma chambers, a deeper and a shallower one, with mass exchange of magma or pressurised liquid between them.

We performed a synthetic data grid search analysis of models with various levels of volume compensation (the explosive component of the first is compensated by the implosive component of the second source) and distances between the system of volume-compensating source and sink. The grid search results showed that given a reasonable uncertainty in source depth, and using imperfect Green's functions with noise, there is a high likelihood that a scenario with a vertically offset horizontal crack and deeper volumetric source will result in a large observed ISO component even with the long period waveforms used. Secondly, it is likely that this large ISO component will also be statistically significant, the opposite from what we observe for the Bárdarbunga earthquake. For example, for two compensating sources at 100% level (where 100% level of compensation means that the explosive component of the first equals to the implosive component of the second source), a grid search parameterization over 1km interval of

source depths and vertical distance between the two sources set to be less or equal to 3km, yields 69 cases. In 59 cases, the obtained isotropic component is higher than 10%. In 41 out of the total number of cases, an isotropic component is resolved; it is statistically significant at 90% level or higher.

Fig. 14 shows an example of the deviatoric and full moment tensor inversion results for a scenario with two compensating sources at the 100% level: an implosion source at 4 km depth and a horizontally opening crack at 2 km depth. The waveforms corresponding to this configuration of sources are produced by the *e3d* finite differences method and are shown by solid lines. 10% of noise was introduced using a random numbers approach, which is comparable in amplitude to the noise level estimated for the Bárdarbunga earthquake. Synthetic waveforms are 1D Green's functions, based on slightly imperfect velocity models (shown by dashed lines) and a depth of 3 km. A large (and significant) ISO component is retrieved from the inversion.

6 DISCUSSION

In the previous section, we described how we used finite differences to produce synthetic finite-source data based on realistic physical scenarios of the event. In moment tensor inversions, 1D modelling is applied to fit the synthetic data. We have not so far discussed to what degree *e3d*-simulated synthetic data waveforms compare with the observed waveforms for the Bárdarbunga earthquake. We compared them quantitatively using cross-correlation on the basis of the best possible fit, after time-shifting waveforms. Overall, cross-correlation coefficients comparing the observed data and *e3d* synthetics at periods between 20 and 50 seconds indicate that the observed data are reproduced in

some cases at the 80% level, but on average only at the 45% level. Fig. 15 shows one such comparison for half-length (Fig. 15a) and full-length rupture (Fig. 15b) for station HOT01 (Fig. 1). Nevertheless, this level of fit is considered to be good given that the finite-difference modelling assumed a simple 1D structure and our moment tensor modelling and other studies have shown a high degree of crustal heterogeneity in the region. Synthetic waveforms are shown for the same range of rupture speeds as shown on abscissa of Fig. 13, from sub-shear to super-shear (black lines) and for the caldera drop event (red lines), and compared directly with the observed waveforms (blue lines) before (left column) and after (right column) time shifting for the best cross-correlation. First, the overall fits are better for the half-length than for the full-length rupture case. Second, it can be seen that no single rupture speed from the range of speeds investigated produces drastically different waveform fits to the observed waveforms, except for the half-length rupture case on the transverse component when the speed approaches infinity (the caldera drop event). As expected, for the full-length rupture case, the infinite speed is not capable of producing net transverse component.

In conclusion, we successfully modelled the Bárdarbunga earthquake with finite rupture processes on a conical surface. The finite-source simulations place bounds on faulting parameters that enable recovery of the observed moment tensor and match the observed seismic waveforms. This is the first time that rupture on a boundary ring fault structure has been modelled as a single seismic event. Although our models are simplified regarding fault geometry, slip distribution (assumed uniform) and rupture velocity (assumed constant) they bracket the range of possible parameters.

Of all the models tested we found that faults much less than half of the cone perimeter

do not produce a sufficiently large CLVD component. For instance, for one quarter-length rupture, the point source inversion produces moment tensors that could be almost fully described as DC with very small CLVD components. The numerical results show that for a moment tensor that is predominantly a vertical CLVD, about half of the ring fault must have ruptured. This is consistent with theoretical results (Frolich 1994; Julian *et al.* 1998). For more than three quarters of full-length rupture at sub-shear speed, the inversion produces poorer fits due to inadequate source duration. Thus, the minimum value of rupture length is required to produce the observed level of the NDC, and the maximum is based on the breakdown of point-source character if the rupture is large and of long duration. Comparisons of the waveforms reveal that sudden collapse of the caldera fault is not a likely model as it fails to generate the observed long-period waves on the transverse component.

For the models involving about half of the full-length circumference there is a general trend in which as rupture speed increases the ability of the moment tensor technique to fit the data and result in mechanisms consistent with the data also increases. This is due to the faster rupture speed resulting in shorter rupture durations that are more consistent with a temporal point source. Although it is not possible to distinguish 180-360˚ ruptures the modelling results indicate that in order to obtain the mechanism and wave-energy ratio consistent with the observations, super-shear rupture velocity is required. In fact the modelling results indicate that rupture speeds in excess of the P-wave speed (along the caldera fault) are possible suggesting a rupture model of dynamic triggering by P-waves directly traversing the interior of the caldera.

While it is possible that two vertically offset volumetric sources can cancel the

volumetric component in the FMT inversion, the circumstances where this can happen are rare, especially where a compensating source of less than 100% is used (the explosive component of the first source is not equal to the implosive component of the second source), or if laterally offset sources are also considered.

ACKNOWLEDGEMENTS

We are grateful to Multimax, Inc. for financial assistance, Dr. Gabi Laske from IGPP, UCSD and the Lawrence Livermore National Laboratory Postdoctoral Program for supporting HT's time on this project, while he was a postdoctoral research fellow at these institutions, and Dr. Shawn Larsen for providing his *e3d* software. Figures were made with the General Mapping Tools (P. Wessel & W. H. F. Smith, 1995 *EOS, Trans. Am. Geophys. Un.,* **76**, 329).

REFERENCES

Allen, R.M., Nolet, G., Morgan, W.J., Vogfjörd, K., Nettles, M., Ekström, G., Bergsson, B.H., Erlendsson, P., Foulger, G.R., Jakobsdóttir, S., Julian, B.R., Pritchard, M., Ragnarsson, S. & Stefánsson, R., 2002. Plume driven plumbing and crustal formation in Iceland, *J. Geophys. Res*., **107**, 10.1029/2001JB000584.

Bouchon, M., Toksöz, M.N., Karabulut, H., Bouin, M.-P., Dietrich, M., Aktar, M. & Edie, M., 2000. Seismic imaging of the Izmit rupture inferred from the near-fault recordings, *Geophys. Res. Lett.*, **27**, 3013-3016.

Bouchon, M. & Vallée, M., 2003. Observation of long supershear rupture during the Ms=8.1 Kunlunshan (Tibet) earthquake, *Science,* **301**, 824-826.

Chouet, B., Dawson, P., Ohminato, T., Martini, M., Saccorotti, G., Giudicepietro, F., De Luca, G., Milana, G. & Scarpa, R., 2003. Source mechanisms of explosions at Stromboli volcano, Italy, determined from moment-tensor inversions of very-long-period data, *J. Geophys. Res.,* **108**, 2019, 10.1029/2002B001919.

Darbyshire, F.A., White, R.S. & Priestley, K.F., 2000. Structure of the crust and uppermost mantle of Iceland from combined seismic and gravity study, *Earth planet. Sci. Lett*., **181**, 409-428.

Dreger, D.S. & Helmberger, D.V., 1993. Determination of source parameters at regional distances with single station or sparse network data, *J. Geophys. Res.,* **98**, 8107-8125.

Dreger, D.S., Tkalčić, H. & Johnston, M., 2000. Dilational processes accompanying earthquakes in the Long Valley Caldera, *Science*, **288**, 122-125.

Dreger, D.S. & Woods, B., 2002. Regional distance seismic moment tensors of nuclear explosions, 2002, *Tectonophysics*, **356**, 139-156.

Du, Z.J. & Foulger, G.R., 1999. The crustal structure of northwest Iceland from receiver functions and surface waves, *Geophys. J. Int.*, **139**, 419-432.

Du, Z.J. & Foulger, G.R., 2001. Variation in the crustal structure across central Iceland, *Geophys. J. Int.*, **145**, 246-264.

Du, Z., Foulger, G.R., Julian, B.R., Allen, R.M., Nolet, G., Morgan, W.J., Bergsson, B.H., Erlendsson, P., Jakobsdottir, S., Ragnarsson, S., Stefansson, R. & Vogfjörd, K., 2002. Crustal structure beneath western and eastern Iceland from surface waves and receiver functions, *Geophys. J. Int.*, **149**, 349-363.

Ekström, G., 1994. Anomalous earthquakes on volcano ring-fault structures, *Earth*

Planet. Sci. Lett., **128**, 707-712.

Ellsworth, W.L., Celebi, M., Evans, J.R., Jensen, E.G., Nyman, D.J. & Spudich, P., 2004. *Proceedings for the 11th International Conference on Soil Dynamics and Earthquake Engineering, Berkeley, CA*, pp 7.

Foulger, G.R. & Long, R.E., 1984. Anomalous focal mechanisms: Tensile crack formation on an accreting plate boundary, *Nature*, **310**, 43-45.

Foulger, G.R., Pritchard, M.J., Julian, B.R., Evans, J.R., Allen, R.M., Nolet, G., Morgan, W.J., Bergsson, B.H., Erlendsson, P., Jakobsdottir, S., Ragnarsson, S., Stefansson, R. & Vogfjörd, K., 2000. The seismic anomaly beneath Iceland extends down to the mantle transition zone and no deeper, *Geophys. J. Int.*, **142**, F1-F5.

Foulger, G.R., Pritchard, M.J., Julian, B.R., Evans, J.R., Allen, R.M., Nolet, G., Morgan, W.J., Bergsson, B.H., Erlendsson, P., Jakobsdottir, S., Ragnarsson, S., Stefansson, R. & Vogfjörd, K., 2001. Seismic tomography shows that upwelling beneath Iceland is confined to the upper mantle, *Geophys. J. Int.*, **146**, 504-530.

Foulger, G.R., Du, Z. and Julian, B.R., 2003. Icelandic-type crust, *Geophys. J. Int.*, **155**, 567-590.

Frohlich, C., 1994. Earthquakes with non-double-couple mechanisms, *Science*, **264**, 804-809.

Julian, B.R., 1983. Evidence for dyke intrusion earthquake mechanisms near Long Valley caldera, California, *Nature,* **303**, 323-325.

Julian, B.R. & Sipkin, S.A., 1985. Earthquake processes in the Long Valley caldera area, California, *J. Geophys. Res*., **90**, 11 155-11 169.

Julian, B.R., 1986. Analysing seismic-source mechanisms by linear programming methods, *Geophys. J. R. astr. Soc*., **84**, 431-443.

Julian, B.R. & Foulger, G.R., 1996. Earthquake mechanisms from linear-programming inversion of seismic-wave amplitude ratios, *Bull. Seismol. Soc. Am*., **86**, 972-980.

Julian, B.R., Miller, A.D. & Foulger, G.R., 1998. Non-double-couple earthquakes: 1. Theory, *Rev. Geophys*., **36**, 525-550.

Kawakatsu, H., 1991. Enigma of earthquakes at ridge-transform fault plate boundaries: Distribution of non-double couple parameter of Harvard CMT solutions, *Geophys. Res. Lett*., **18**, 1103-1106.

Konstantinou, I.K., Kao, H., Lin, C.-H. & Liang, W.-T., 2003. Analysis of broad-band regional waveforms of the 1996 September 29 earthquake at Bárdarbunga volcano, central Iceland: investigation of the magma injection hypothesis, *Geophys. J. Int*., **154**, 134-145.

Kostrov, B. & Das, S., 1989. *Principles of Earthquake Source Mechanics,* Cambridge Univ. Press, Cambridge, UK.

Kuge, K. & Lay, T., 1994. Systematic non-double-couple components of earthquake mechanisms: The role of fault zone irregularity, *J. Geophys Res.*, **99**, 15 457-15 467.

Larsen, S.C. & Schultz, C.A., 1995. ELAS3D: 2D/3D elastic finite-difference wave propagation code, Technical Report No. UCRL-MA-121792, 19 pp.

Levander, A.R., 1988. Fourth-order finite-difference P-SV seismograms, *Geophysics*, **53**, 1425-1436.

Madariaga, R., 1976. Dynamics of an expanding circular fault, *Bull. Seismol. Soc. Am*.,

66, 639-667.

Nettles, M. & Ekström, G., 1998. Faulting mechanism of anomalous earthquakes near Bárdarbunga volcano, Iceland, *J. Geophys. Res.,* **103,** 17 973-17 983.

Panning, M., Dreger, D.S. & Tkalčić, H., 2001. Near-source structure and isotropic moment tensors: a case study of the Long Valley Caldera, *Geophys. Res. Lett*., **28,** 1815-1818.

Pasyanos, M.E., Dreger, D.S. & Romanowicz, B., 1996. Towards real-time determination of regional moment tensor, *Bull. Seismol. Soc. Am*., **86**, 1255-1269.

Virieaux, J., 1986. P-SV wave propagation in heterogeneous media: velocity-stress finite-difference method, *Geophysics*, **51**, 889-901.

FIGURE CAPTIONS

Figure 1. Map showing the main tectonic and volcanic features in Iceland. Glaciers are shown in white and spreading segments (volcanic systems) are shown in dark gray. Volcanoes are shown by thin solid lines. The Bárdarbunga earthquake estimated location is represented by the white star. Triangles are locations of six Iceland Hotspot Project broadband stations used in the moment tensor and finite difference simulations.

Figure 2. Comparison of **(a)** deviatoric and **(b)** full moment tensor point-source inversion results for the Bárdarbunga event. Three-component displacement seismograms (radial, vertical and tangential, from left to right) are shown by solid lines and compared to 1D-synthetic seismograms (dashed lines). The lower-hemisphere projection of the P-wave radiation pattern is shown on the right. The strike, rake and dip of the two nodal planes of the best DC solution, as well as the scalar seismic moment, moment magnitude, and percentage DC, CLVD and ISO, are given numerically at right.

Figure 3. As for Fig. 1 but results for point-source moment tensor inversion for another, independent set of stations, excluding those shown in Fig. 2.

Figure 4. Jackknife sensitivity test, illustrating the stability of **(a)** the CLVD, presented by the value of ε, where ε is a measure of the size of the CLVD component relative to the DC and λ_i are the deviatoric eigenvalues of M_{ij}; **(b)** the ISO components, as a function of the number of stations used in the inversion. The symbols show the mean percent ISO ± 1 standard deviation (error bars).

Figure 5. Schematic representation of the conical geometry of the caldera ring fault and equidistant point sources used to simulate finite processes.

Figure 6. Variance reduction results for 24 various orientations (dipping angles) of the outward-dipping caldera ring fault, and various portions of the rupture. Finite source, finite-difference waveforms are used as synthetic data and 1-D Greens functions are used as synthetics to fit the data in a point-source time-domain MT inversion.

Figure 7. Same as Fig. 6 but showing the focal mechanism results. The number above each "beach ball" indicates percentage of CLVD.

Figure 8. As Fig. 2 but showing **(a)** deviatoric MT point-source inversion results for finite-source synthetics used as the synthetic data and 1D Green's functions used to fit the data, assuming the half-length rupture scenario. Three-component (transverse, radial and vertical) displacement data (solid line) are fit by the 1D synthetic seismograms (dashed line). **(b)** Deviatoric MT point-source inversion results for a reverse mechanism synthetics used as synthetic data and 1D synthetic seismograms.

Figure 9. As Fig. 2 but showing the deviatoric MT inversion results using the model of a full-length rupture of the caldera at the same rupture speed as used in the inversion shown in Figure 2b (3.9 km/s). Note the opposite sign of the CLVD and poor fits to the waveforms.

Figure 10. As Fig. 2 but showing the deviatoric MT inversion results using the model of a bilateral full-length rupture of the caldera at the rupture speed of 3.9 km/s.

Figure 11. As Fig. 2 but showing the deviatoric inversion results using the model of a quarter-length rupture of the caldera at the rupture speed of 3.9 km/s. The moment tensor has a dominant DC character.

Figure 12. As Fig. 2 but showing the deviatoric MT inversion results using the model of an instantaneous caldera collapse (drop) scenario. Significant amplitudes on the tangential components are not excited, which is not in agreement with the observed waveforms for the earthquake.

Figure 13. Focal mechanisms, variance reduction (numbers above "beach balls") and normalized H/V seismic wave energy ratio (diamonds) plotted as a function of rupture speed for half-length caldera rupture simulations. Normalized H/V energy from the Bárdarbunga earthquake waveforms is shown by stars. INF: infinitively large speed of rupture (caldera collapse).

Figure 14. As Fig. 2 but showing **(a)** the deviatoric and **(b)** full moment tensor inversions using the model of two compensating sources at the 100% level (volumetric exchange equal and opposite in sign), an implosion source at 4 km depth and a horizontally opening crack at 2 km depth. The waveforms corresponding to these sources are shown by solid lines and are used as synthetic data. 10% noise is included. The modelled waveforms are 1D Green's functions, based on slightly imperfect velocity models (shown by dashed lines) and a depth of 3 km.

Figure 15. Finite-differences-generated synthetics at station HOT01 assuming the same range of rupture speeds as shown on the abscissa of Fig. 13, from sub-shear to super-

shear (black lines) and for the caldera drop event (red lines), for **(a)** half-length and **(b)** full-length rupture. Bárdarbunga earthquake waveforms (blue lines) are compared directly with the synthetics before (left column) and after (right column) time-shifting for the best cross-correlation.

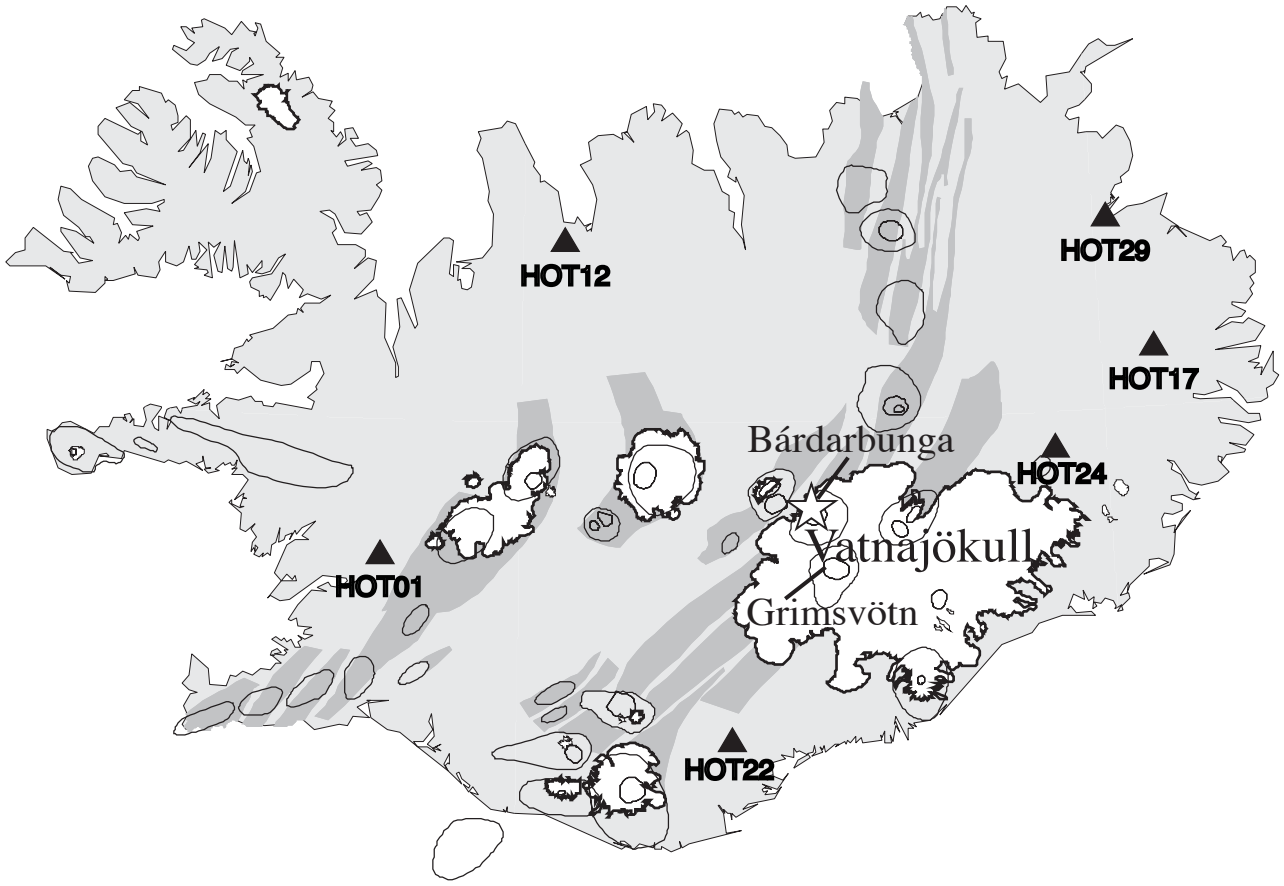
HOT12
HOT29
HOT17
Bárdarbunga
HOT24
Vatnajökull
HOT01
Grímsvötn
HOT22

Figure 1

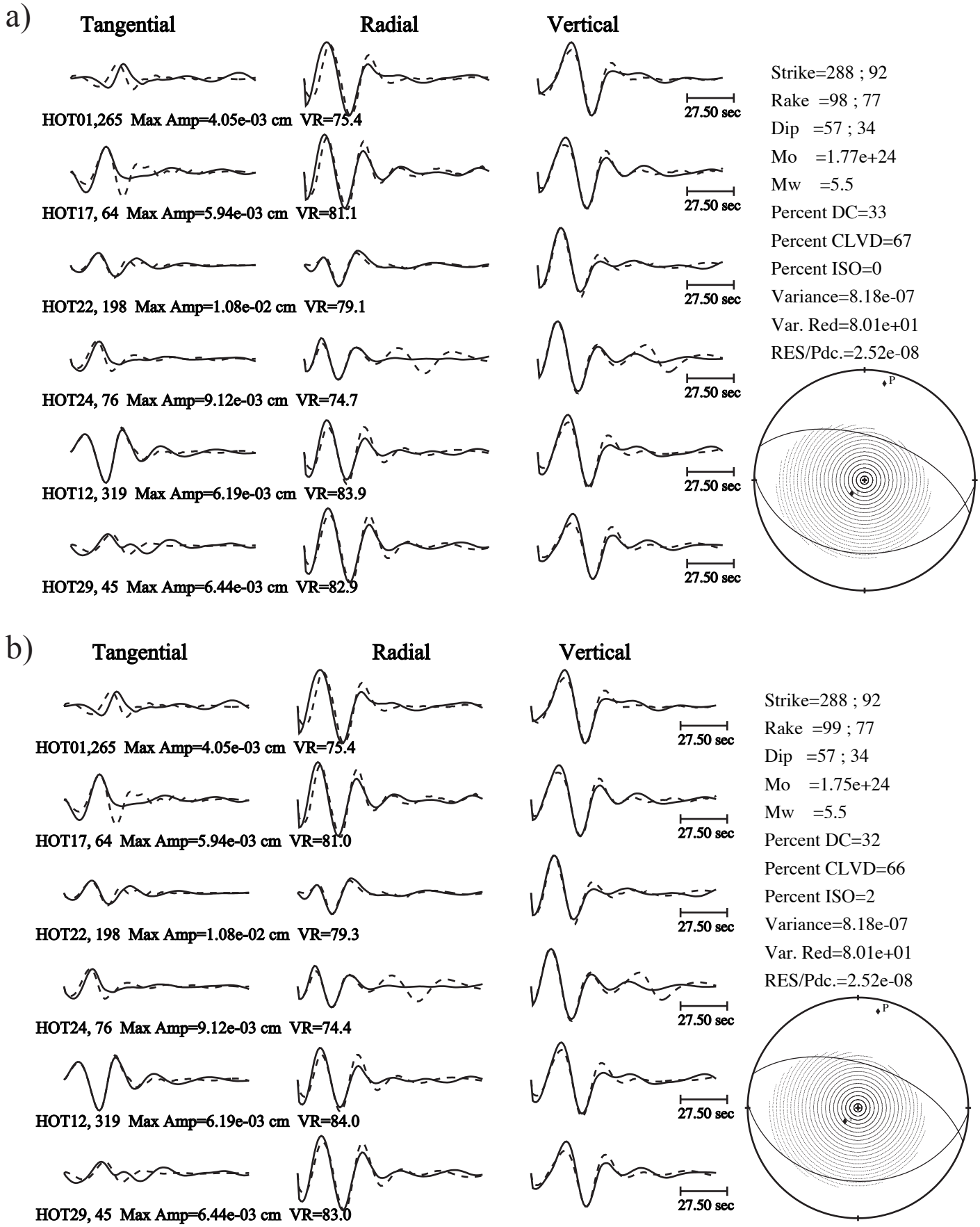
a)
Tangential
Radial
Vertical
HOT01,265 Max Amp=4.05e-03 cm VR=75.4
HOT17, 64 Max Amp=5.94e-03 cm VR=81.1
HOT22, 198 Max Amp=1.08e-02 cm VR=79.1
HOT24, 76 Max Amp=9.12e-03 cm VR=74.7
HOT12, 319 Max Amp=6.19e-03 cm VR=83.9
HOT29, 45 Max Amp=6.44e-03 cm VR=82.9
27.50 sec
Strike=288 ; 92
Rake =98 ; 77
Dip =57 ; 34
Mo =1.77e+24
Mw =5.5
Percent DC=33
Percent CLVD=67
Percent ISO=0
Variance=8.18e-07
Var. Red=8.01e+01
RES/Pdc.=2.52e-08
P
b)
Tangential
Radial
Vertical
HOT01,265 Max Amp=4.05e-03 cm VR=75.4
HOT17, 64 Max Amp=5.94e-03 cm VR=81.0
HOT22, 198 Max Amp=1.08e-02 cm VR=79.3
HOT24, 76 Max Amp=9.12e-03 cm VR=74.4
HOT12, 319 Max Amp=6.19e-03 cm VR=84.0
HOT29, 45 Max Amp=6.44e-03 cm VR=83.0
27.50 sec
Strike=288 ; 92
Rake =99 ; 77
Dip =57 ; 34
Mo =1.75e+24
Mw =5.5
Percent DC=32
Percent CLVD=66
Percent ISO=2
Variance=8.18e-07
Var. Red=8.01e+01
RES/Pdc.=2.52e-08
P

Figure 2

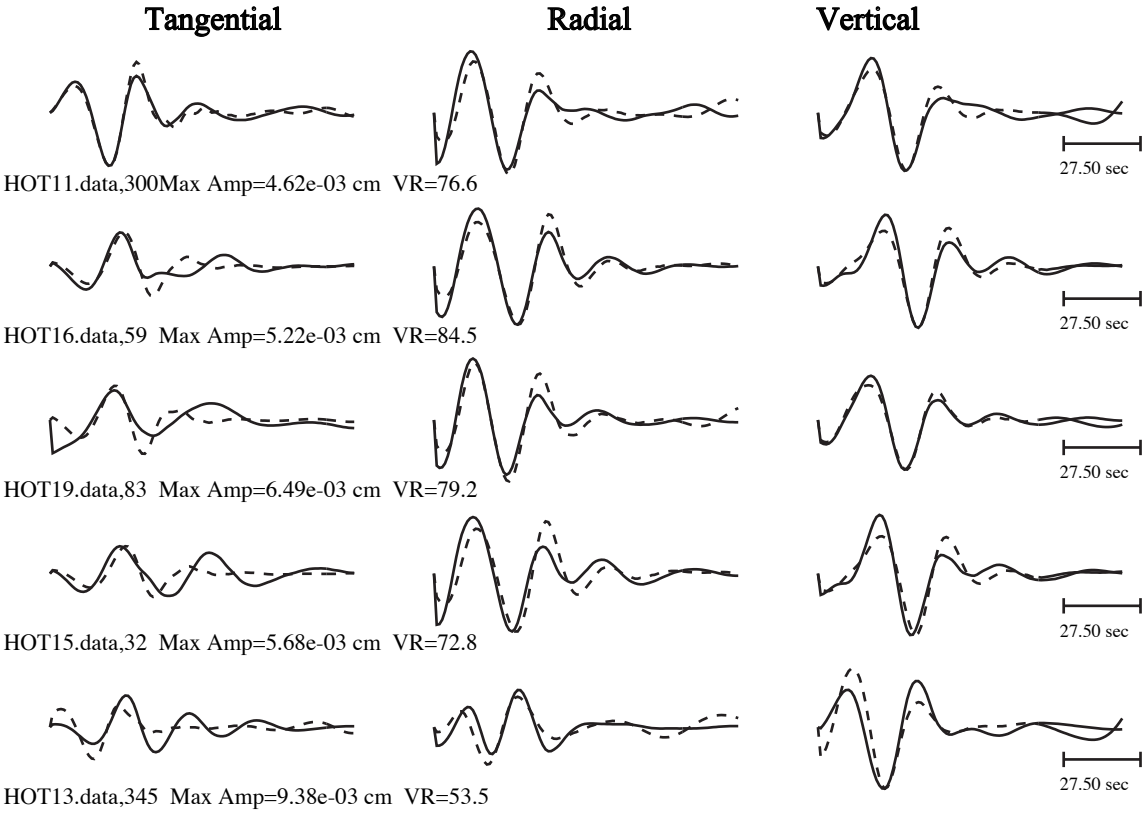

Strike=299 ; 101
Rake =100 ; 75
Dip =56 ; 35
Mo =1.74e+24
Mw =5.5
Percent DC=36
Percent CLVD=64
Percent ISO=0
Variance=1.10e-06

Var. Red=7.25e+01
RES/Pdc.=3.08e-08

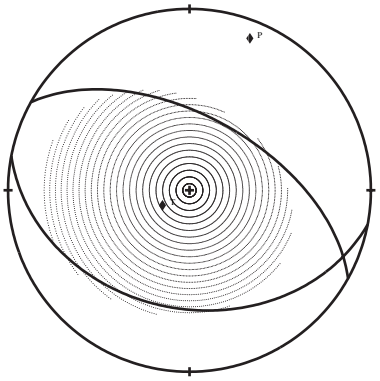

Figure 3

a)

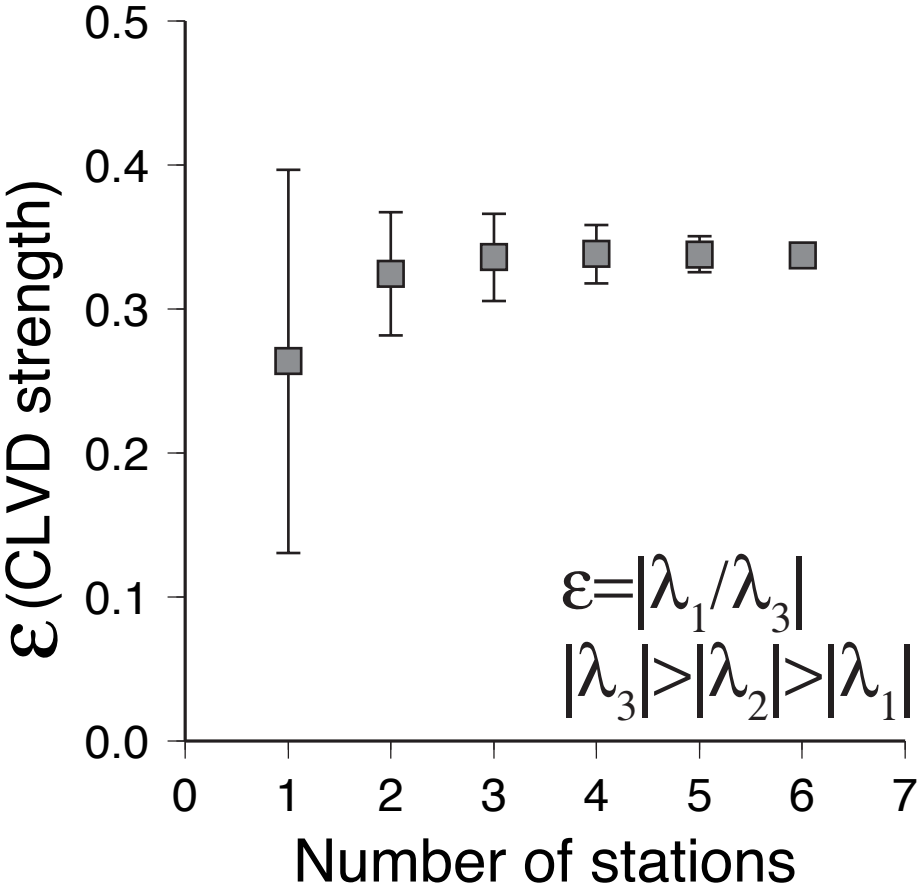
0.5
0.4
0.3
0.2
0.1
0.0
ε (CLVD strength)
ε=|λ1/λ3|
|λ3|>|λ2|>|λ1|
0
1
2
3
4
5
6
7
Number of stations

b)

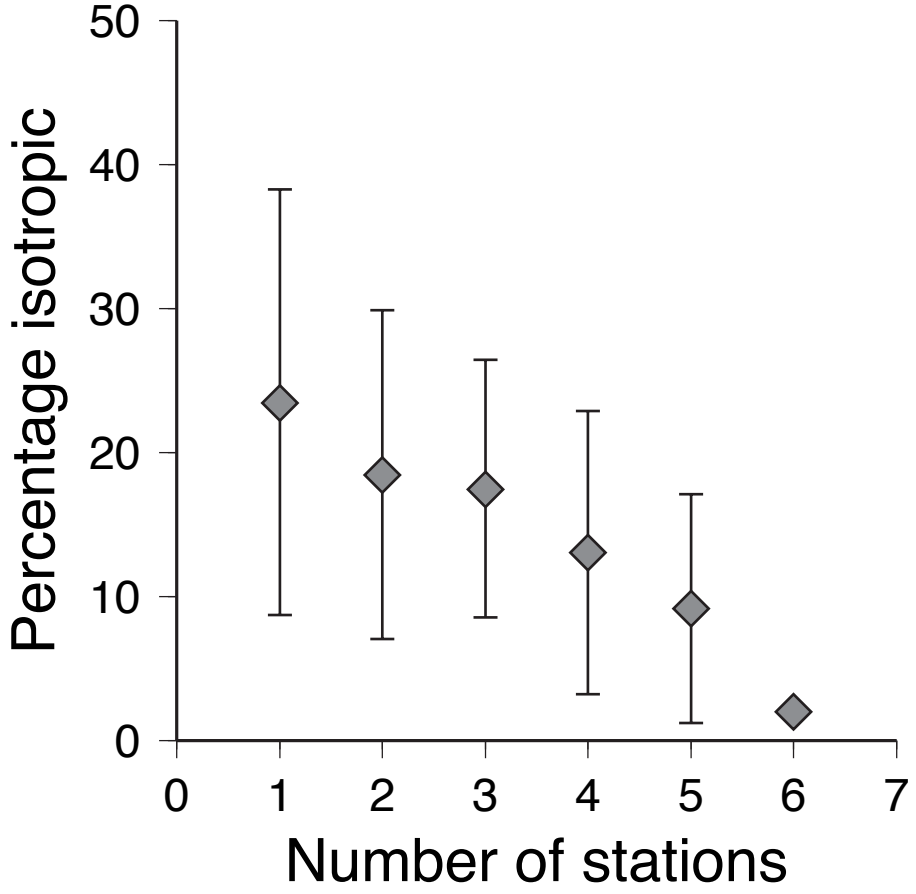
50
40
30
20
10
0
Percentage isotropic
0
1
2
3
4
5
6
7
Number of stations

Figure 4

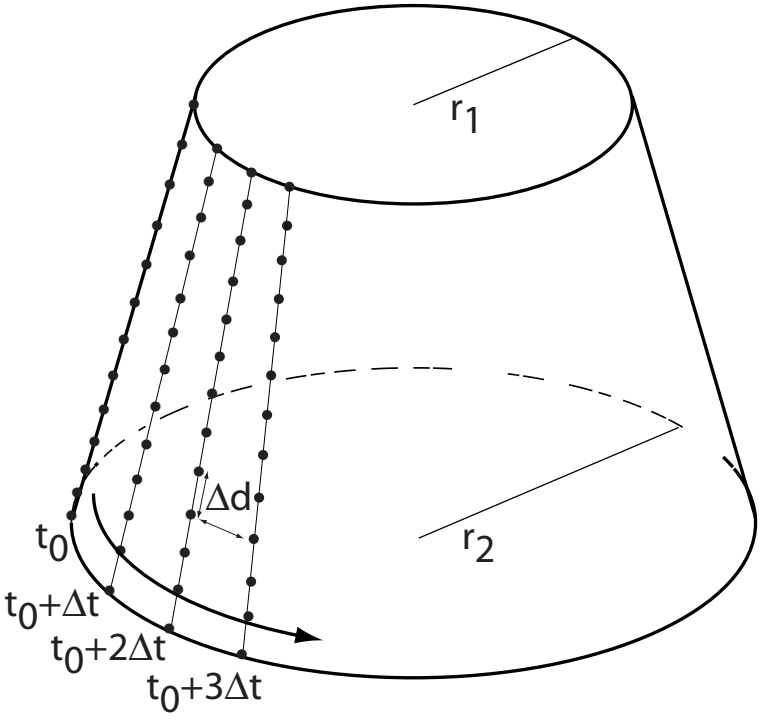

Figure 5

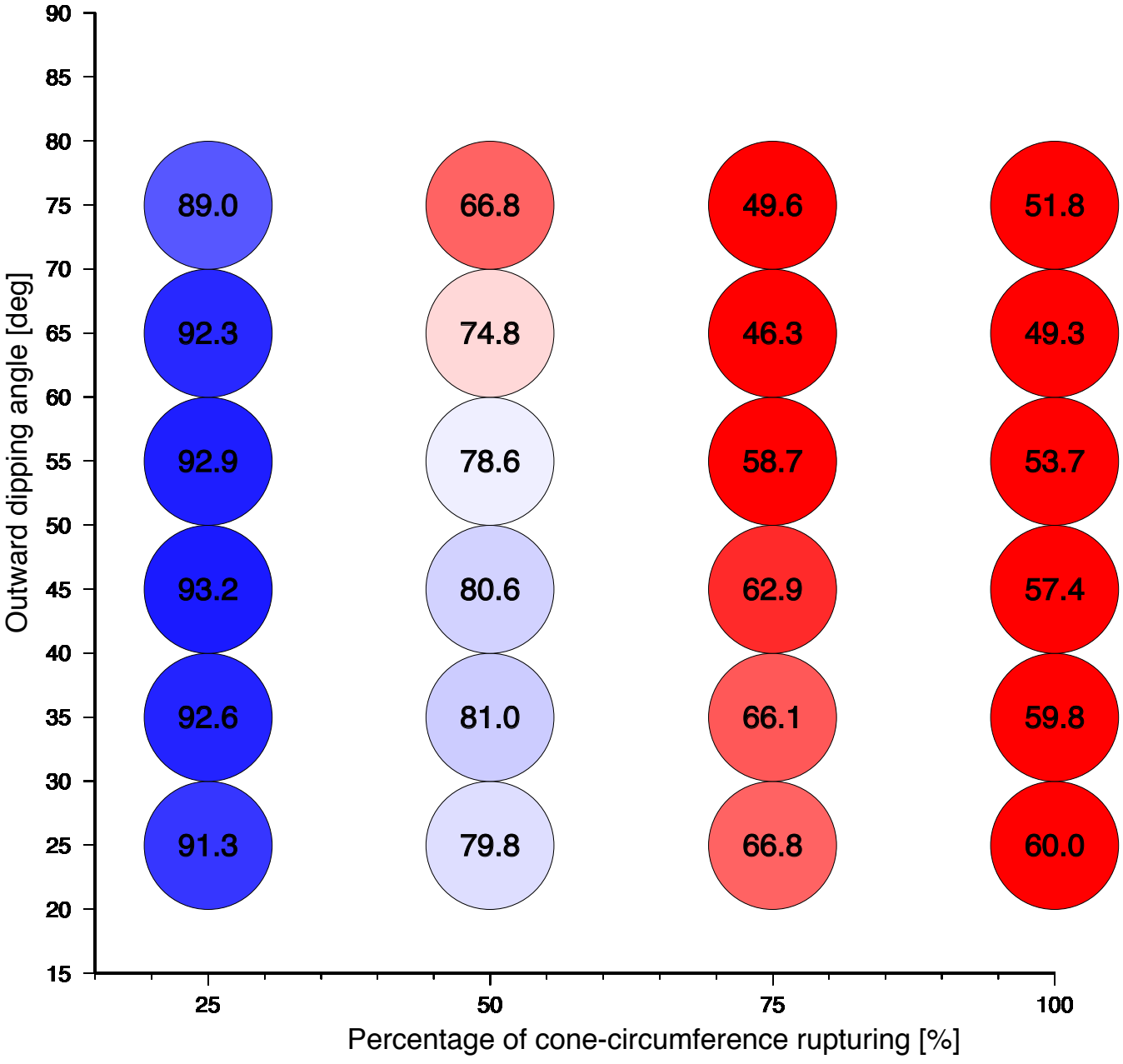

Starting point: 90° east of north on a circular fault
Synthetics from 6 stations are matched with Green's functions
Rupture speed = 3.1km/s
The dipping angle - angle between the base of the cone and its wall

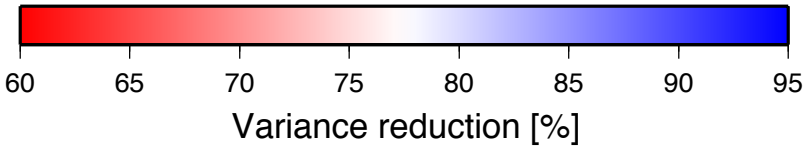

Figure 6

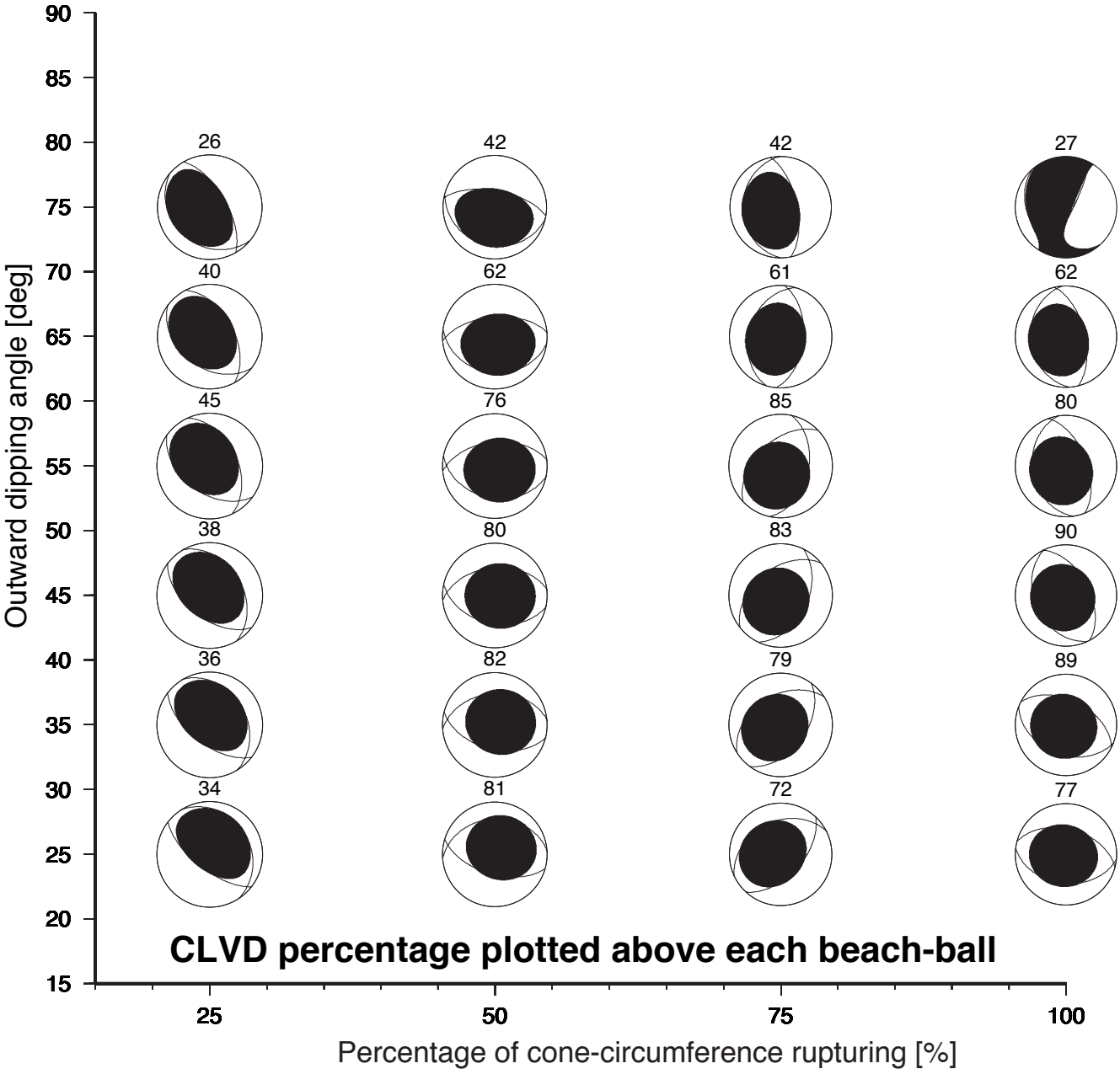

Starting point: 90º east of north on a circular fault
Synthetics from 6 stations are matched with Green's functions
Rupture speed = 3.1km/s
The dip. angle - angle between the base of the cone and its wall

Figure 7

a)

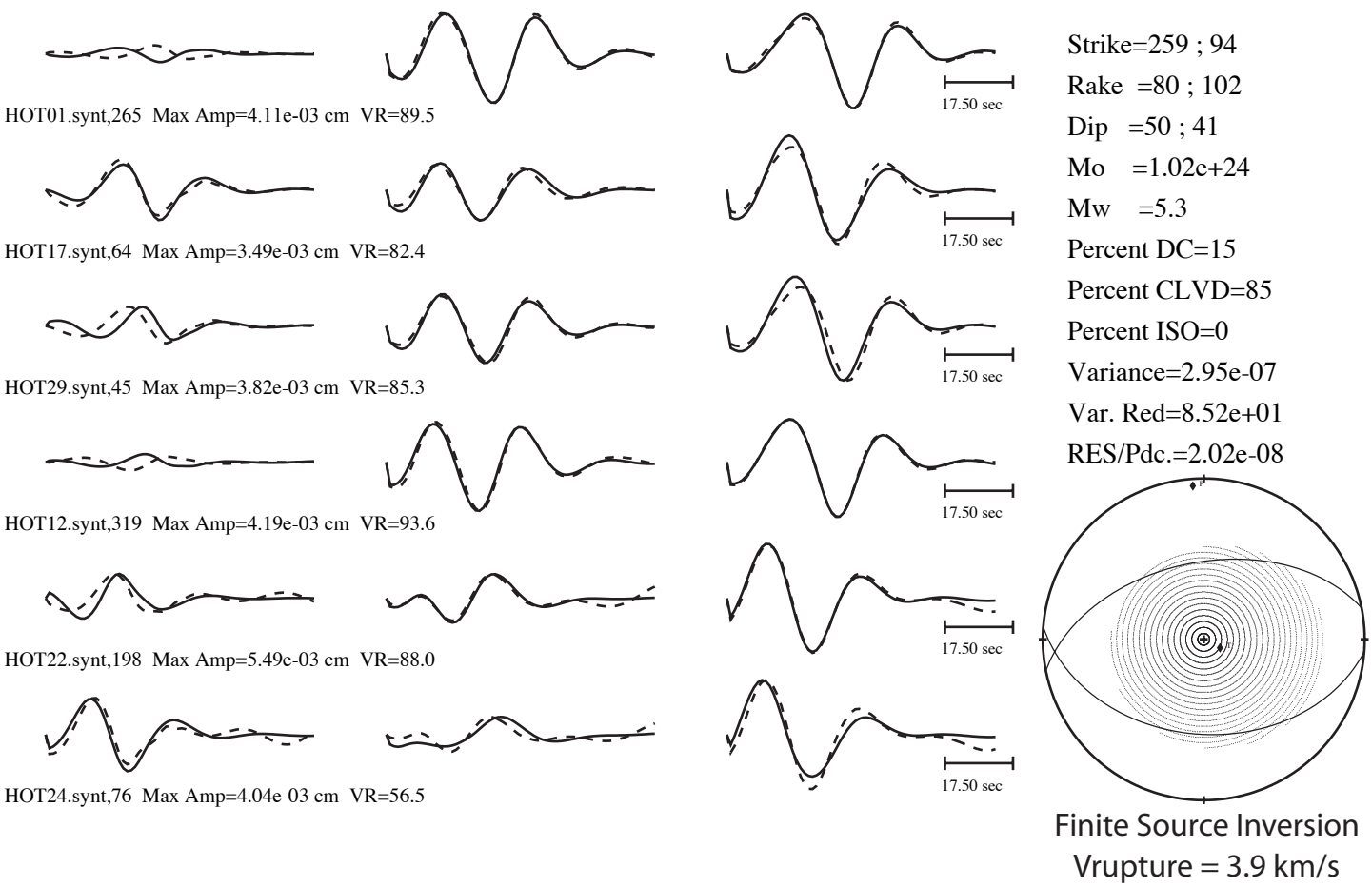
Tangential
Radial
Vertical
HOT01.synt,265 Max Amp=4.11e-03 cm VR=89.5
HOT17.synt,64 Max Amp=3.49e-03 cm VR=82.4
HOT29.synt,45 Max Amp=3.82e-03 cm VR=85.3
HOT12.synt,319 Max Amp=4.19e-03 cm VR=93.6
HOT22.synt,198 Max Amp=5.49e-03 cm VR=88.0
HOT24.synt,76 Max Amp=4.04e-03 cm VR=56.5
17.50 sec
Strike=259 ; 94
Rake =80 ; 102
Dip =50 ; 41
Mo =1.02e+24
Mw =5.3
Percent DC=15
Percent CLVD=85
Percent ISO=0
Variance=2.95e-07
Var. Red=8.52e+01
RES/Pdc.=2.02e-08
Finite Source Inversion
Vrupture = 3.9 km/s

b)

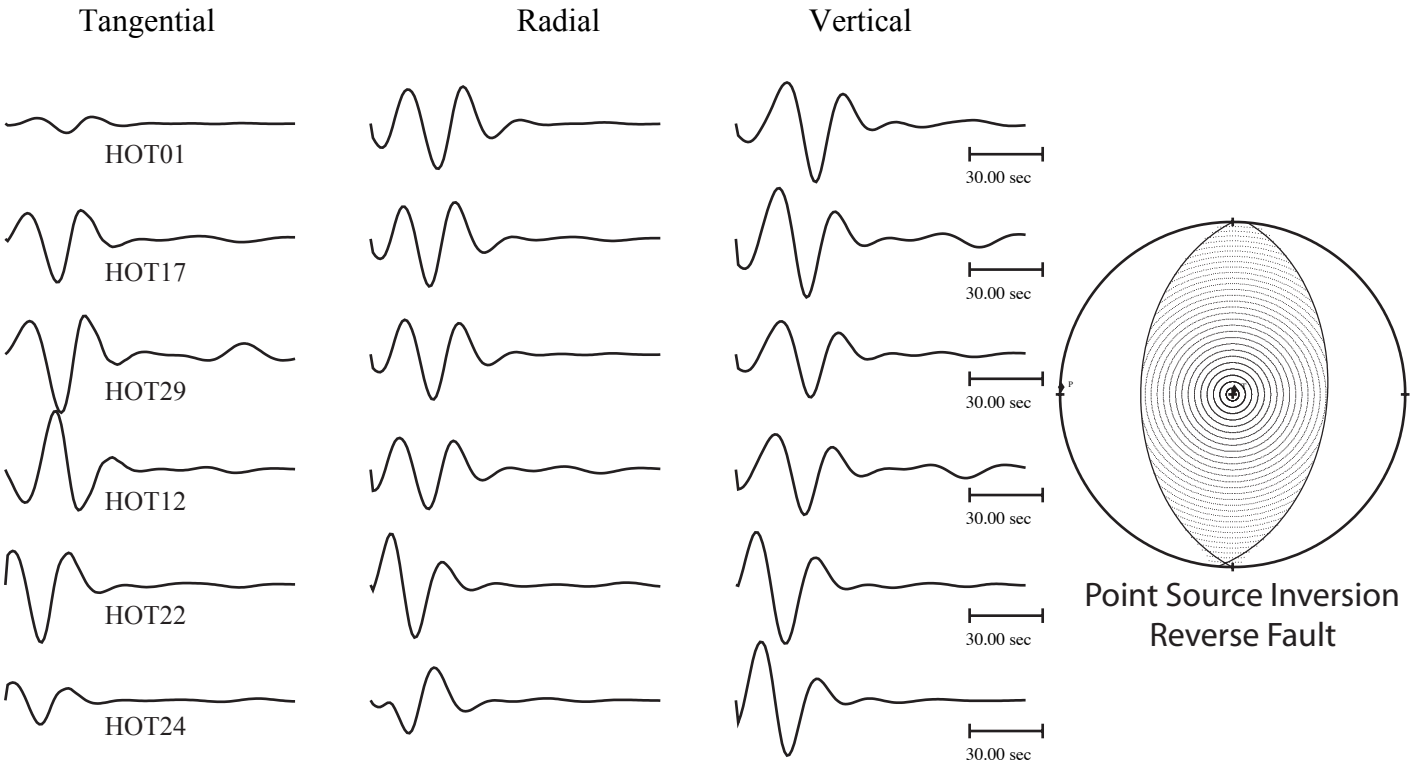
Tangential
Radial
Vertical
HOT01
HOT17
HOT29
HOT12
HOT22
HOT24
30.00 sec
Point Source Inversion
Reverse Fault

Figure 8

Full-Length Caldera Unilateral Rupture

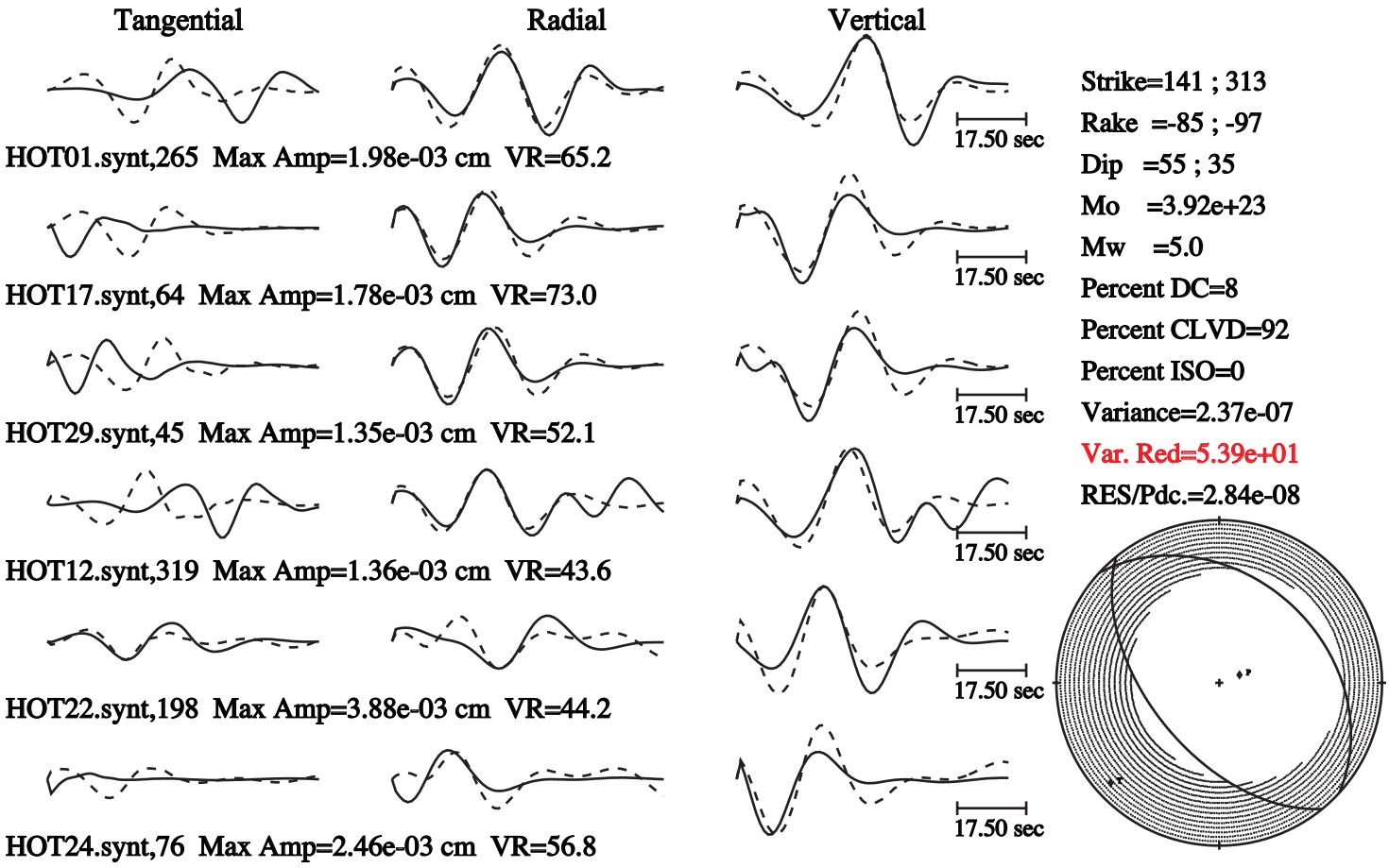

Figure 9

Full-Length Caldera Bilateral Rupture

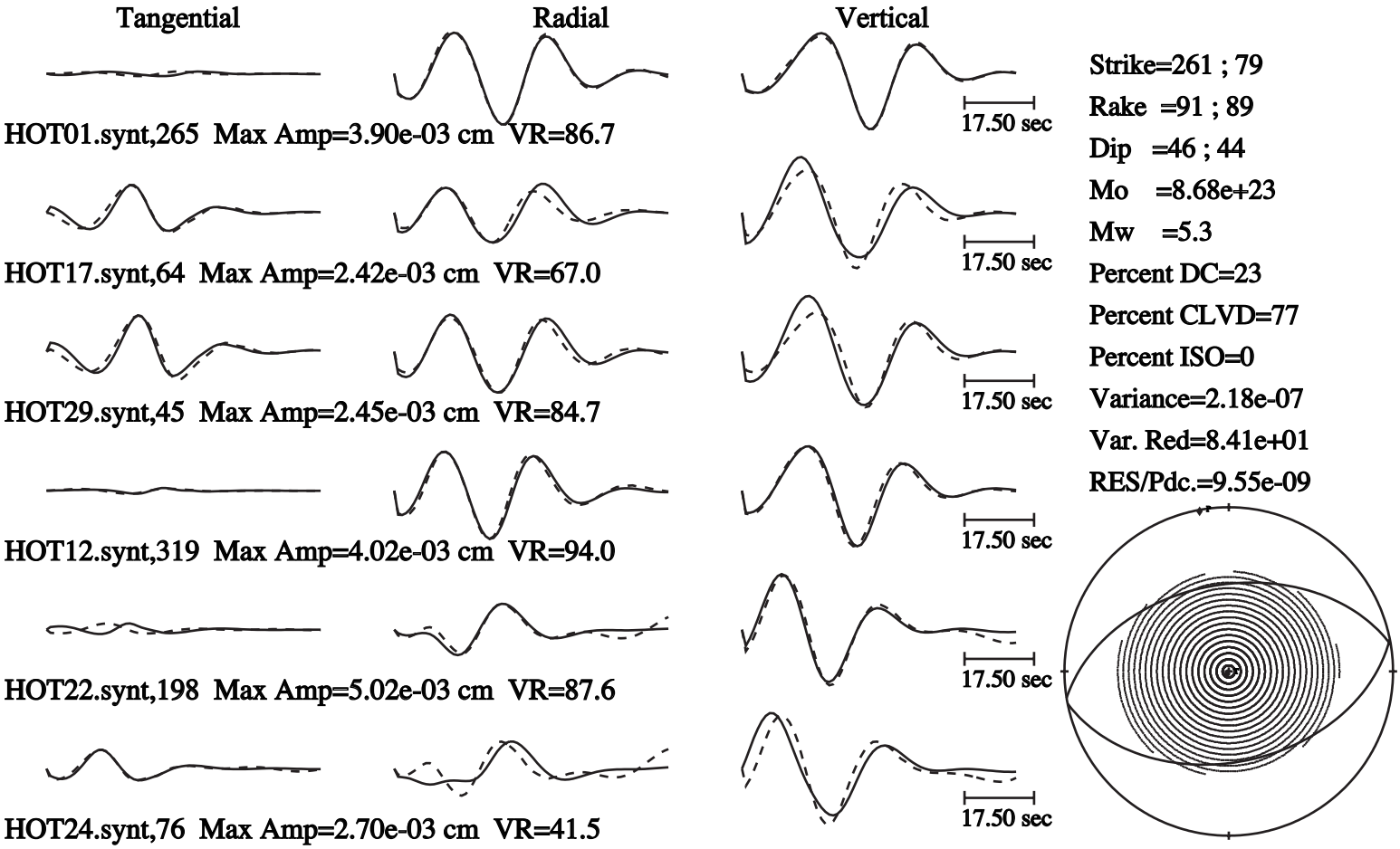

Figure 10

Quarter-Length Caldera Unilateral Rupture

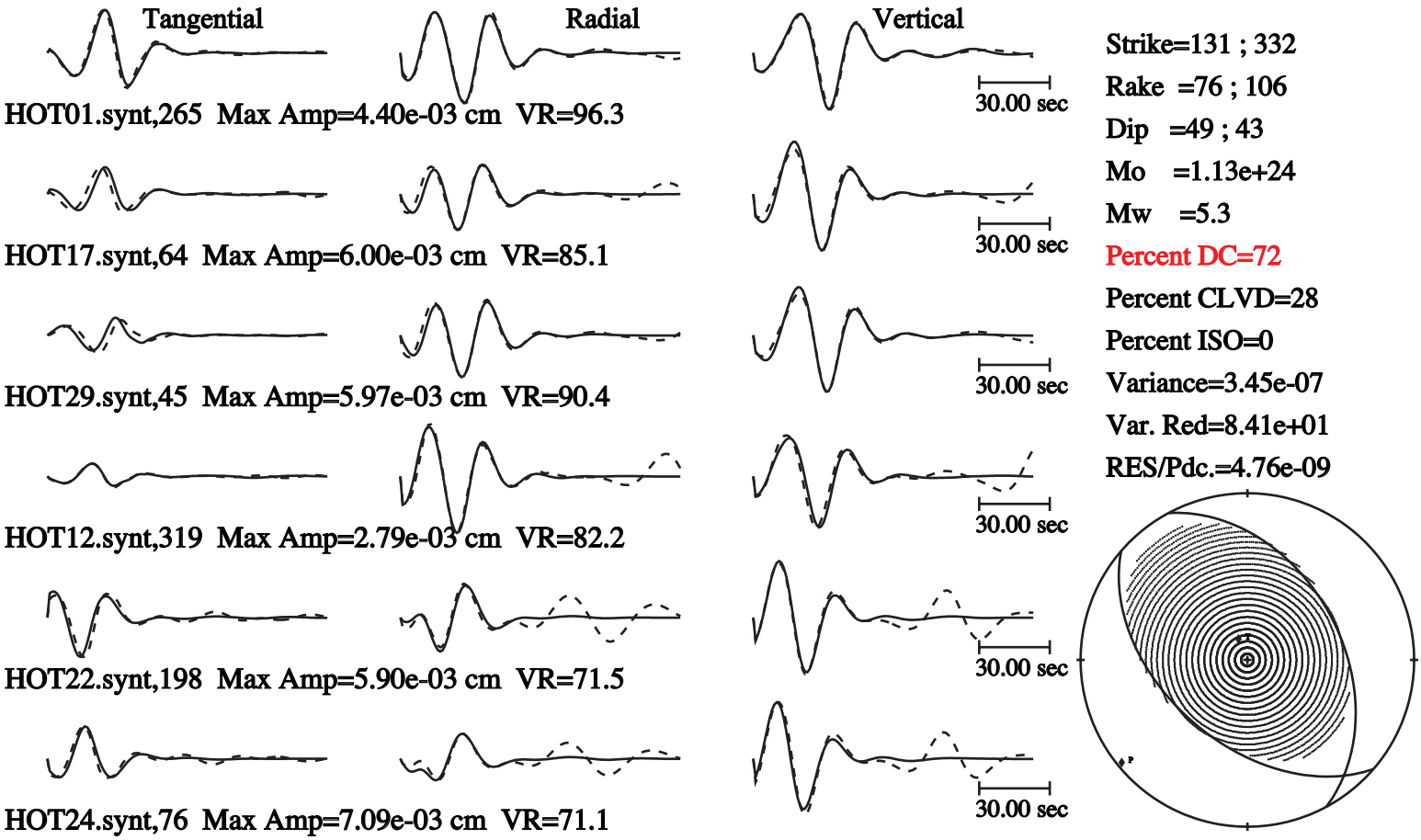

Figure 11

“Caldera Drop”

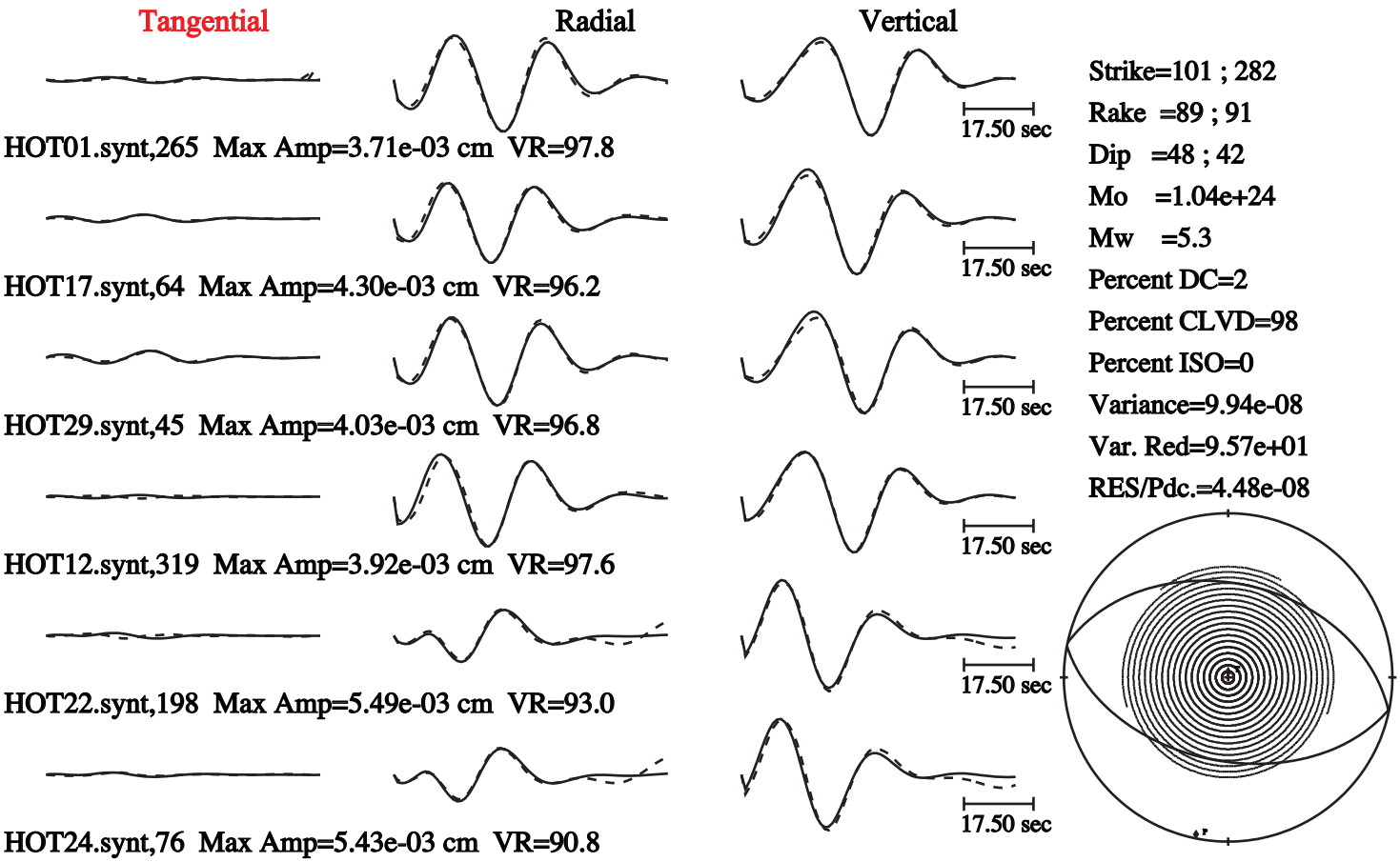

Figure 12

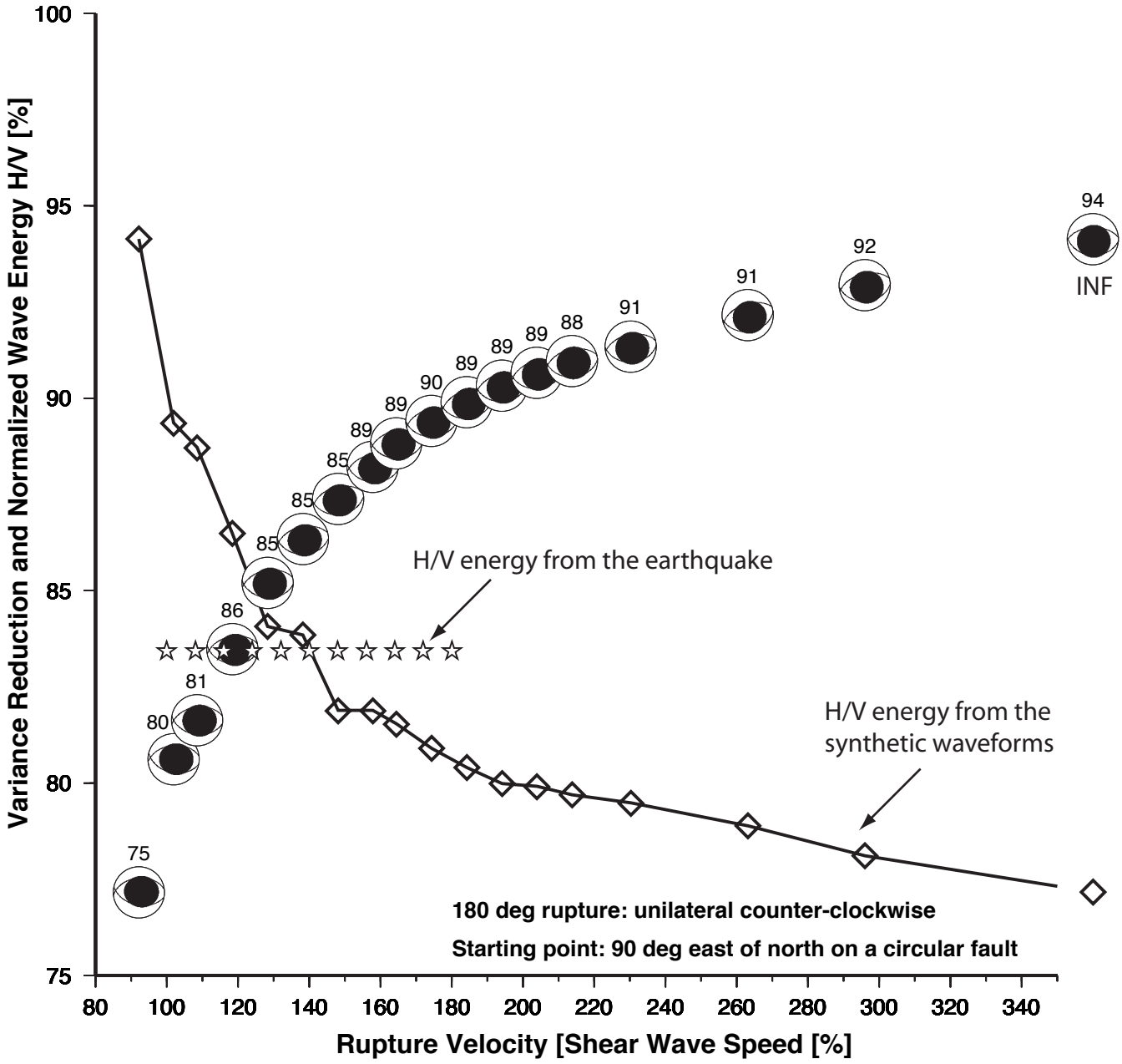
Variance Reduction and Normalized Wave Energy H/V [%]
Rupture Velocity [Shear Wave Speed [%]
100
95
90
85
80
75
80
100
120
140
160
180
200
220
240
260
280
300
320
340
94
INF
92
91
91
89
88
89
89
90
89
89
85
85
85
86
81
80
75
H/V energy from the earthquake
H/V energy from the synthetic waveforms
180 deg rupture: unilateral counter-clockwise
Starting point: 90 deg east of north on a circular fault

Figure 13

a)

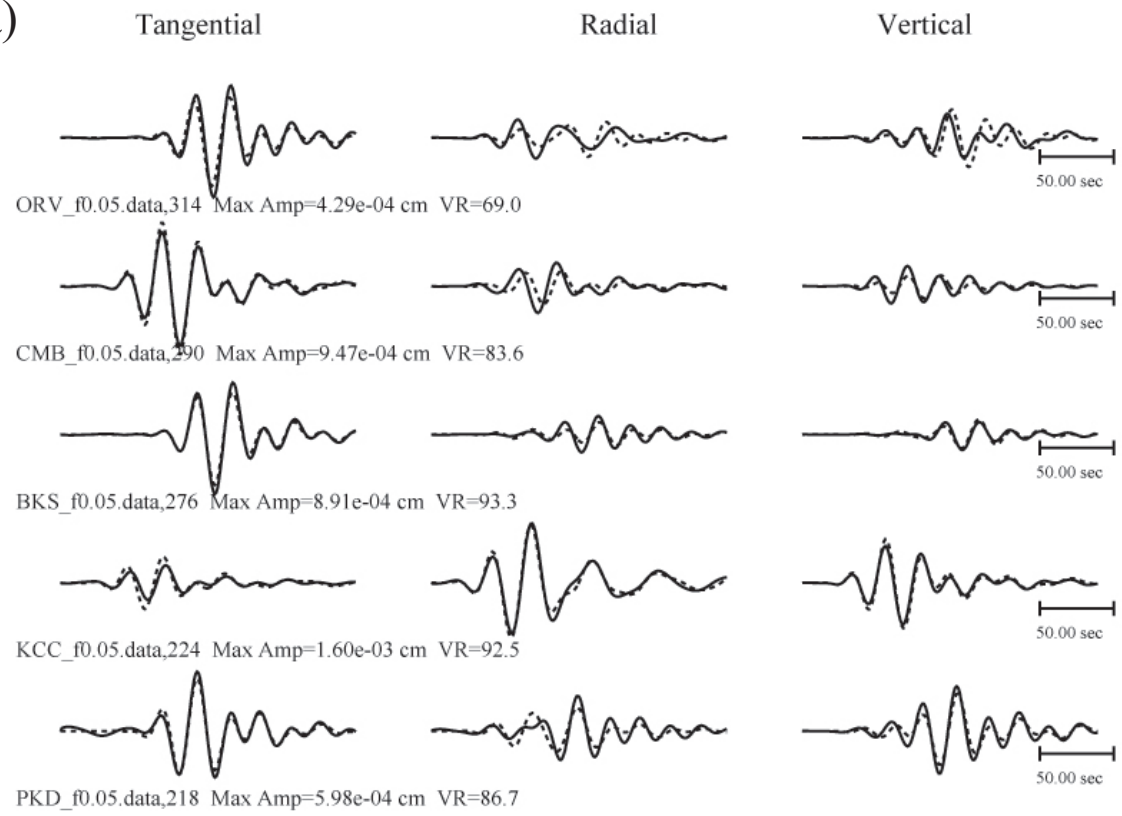

Strike=182 ; 286
Rake =-51 ; -162
Dip =78 ; 41
Mo =2.02e+23
Mw =4.8
Percent DC=59
Percent CLVD=41
Percent ISO=0
Variance=4.29e-09
Var. Red=8.80e+01
RES/Pdc.=7.27e-11

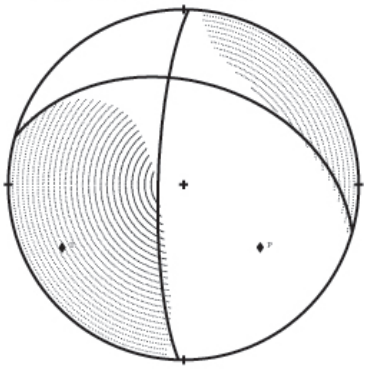

b)

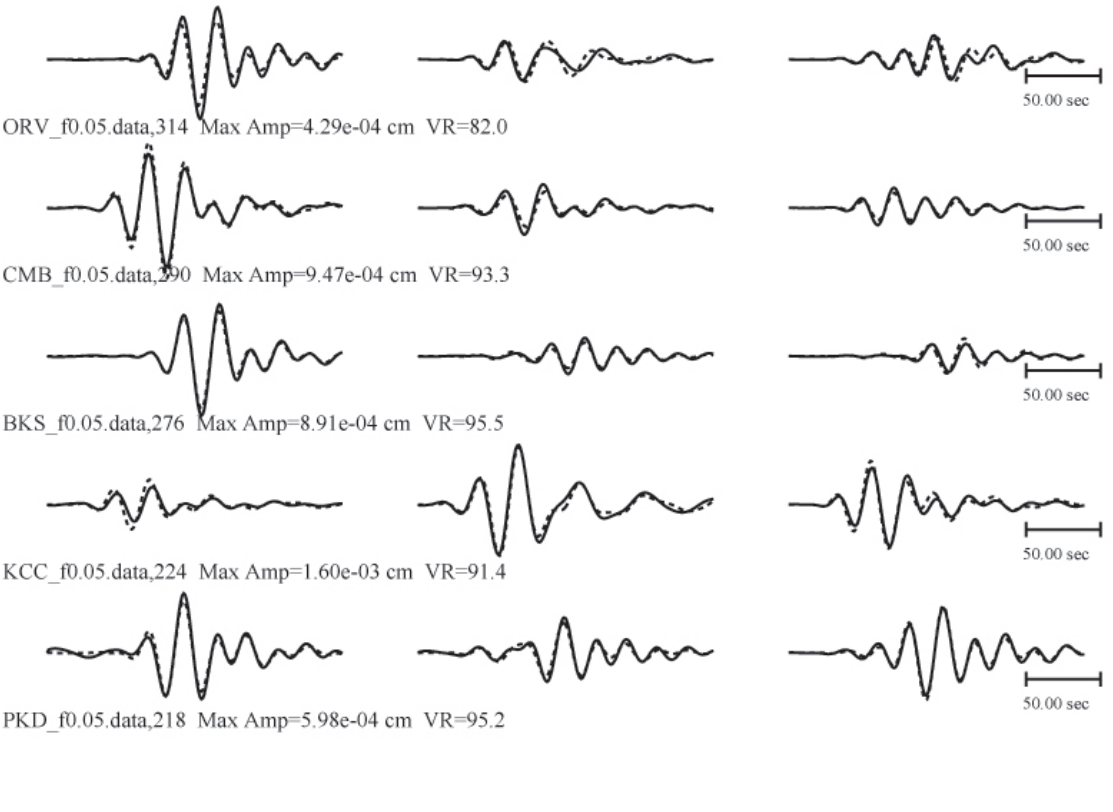

Strike=24 ; 268
Rake =52 ; 146
Dip =68 ; 43
Mo =2.32e+23
Mw =4.9
Percent DC=60
Percent CLVD=0
Percent ISO=40
Variance=3.29e-09
Var. Red=9.29e+01
RES/Pdc.=5.47e-11

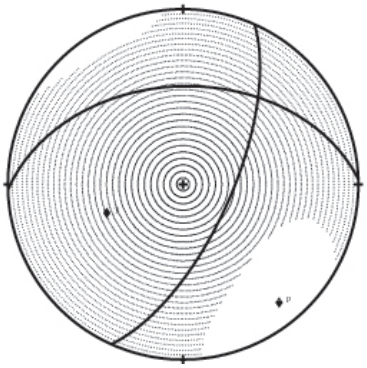

Figure 14

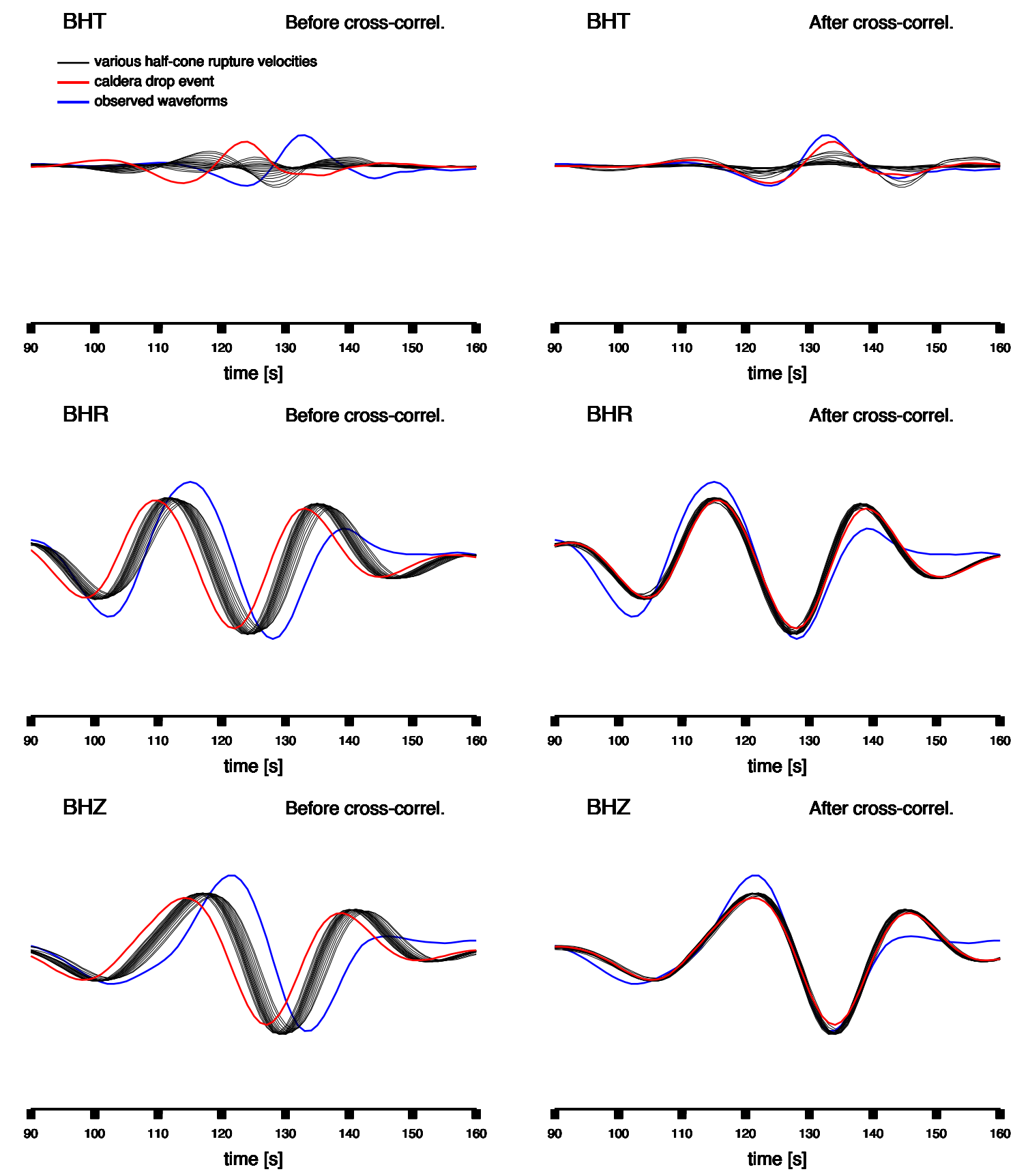
a)
HOT01 half-length rupture
BHT
Before cross-correl.
BHT
After cross-correl.
various half-cone rupture velocities
caldera drop event
observed waveforms
90 100 110 120 130 140 150 160
time [s]
BHR
Before cross-correl.
BHR
After cross-correl.
BHZ
Before cross-correl.
BHZ
After cross-correl.

Figure 15

b)

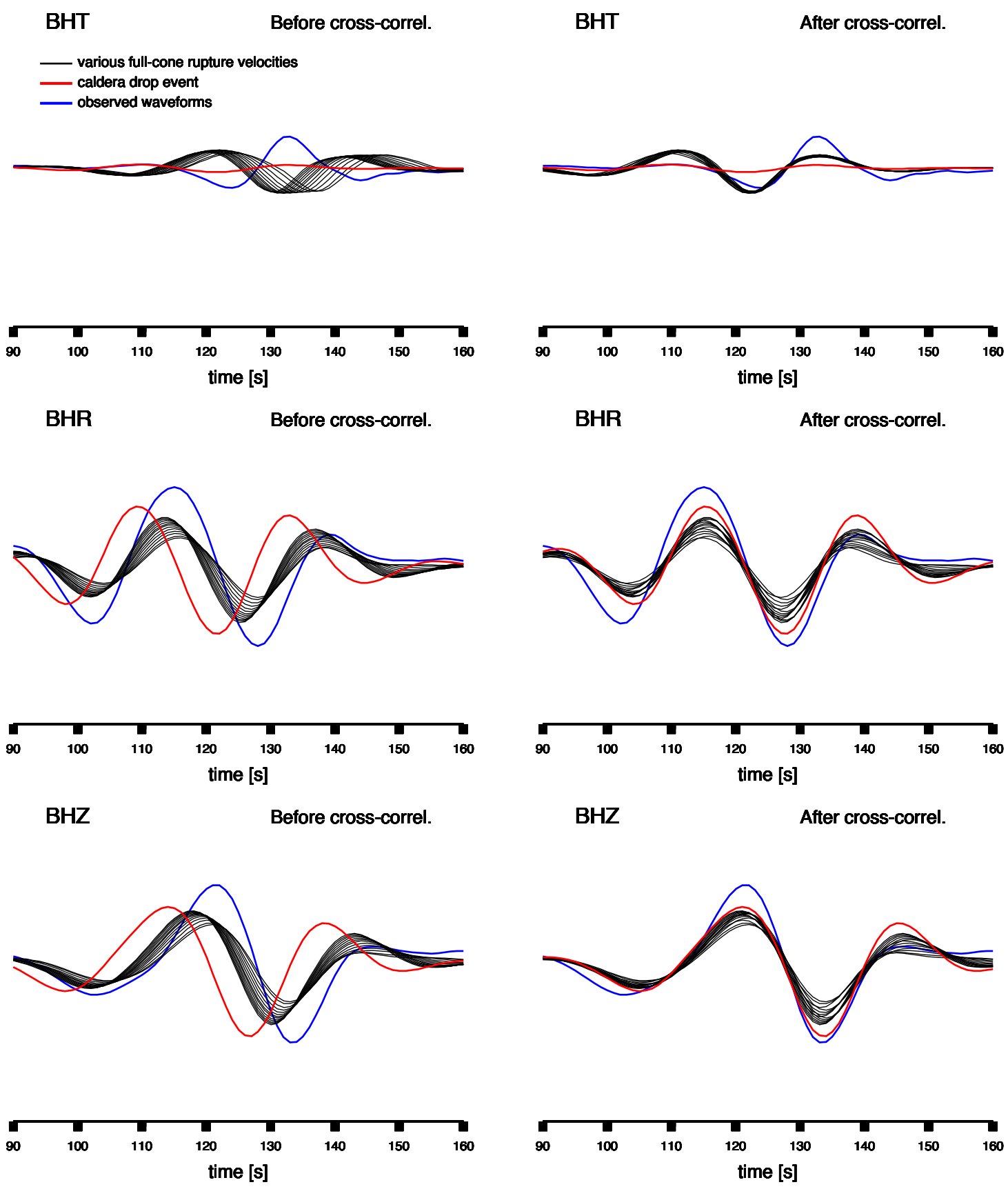

Figure 15 contd.